Monthly Notices of the ROYAL ASTRONOMICAL SOCIETY

MNRAS **441,** 316–332 (2014) doi:10.1093/mnras/stu572

The nature of massive black hole binary candidates – II. Spectral energy distribution atlas

E. Lusso,[1⋆] R. Decarli,[1] M. Dotti,[2,3] C. Montuori,[4,5] David W. Hogg,[1,6] P. Tsalmantza,[7] M. Fumagalli[8,9†] and J. X. Prochaska[10]

[1]*Max Planck Institut für Astronomie, Königstuhl 17, D-69117 Heidelberg, Germany*
[2]*Dipartimento di Fisica G. Occhialini, Università degli Studi di Milano Bicocca, Piazza della Scienza 3, I-20126 Milano, Italy*
[3]*INFN, Sezione Milano-Bicocca, Piazza della Scienza 3, I-20126 Milano, Italy*
[4]*Department of Physics, Technion, IL-32000 Haifa, Israel*
[5]*Dipartimento di Scienza e Alta Tecnologia, Università dell' Insubria, via Valleggio 11, I-22100 Como, Italy*
[6]*Center for Cosmology and Particle Physics, Department of Physics, New York University, 4 Washington Place, New York, NY 10003, USA*
[7]*Klausenpfad 22, Heidelberg, D-691221, Germany*
[8]*Carnegie Observatories, 813 Santa Barbara Street, Pasadena, CA 91101, USA*
[9]*Department of Astrophysics, Princeton University, Princeton, NJ 08544-1001, USA*
[10]*Department of Astronomy and Astrophysics, UCO/Lick Observatory, University of California, 1156 High Street, Santa Cruz, CA 95064, USA*

Accepted 2014 March 19. Received 2014 March 4; in original form 2014 January 17

ABSTRACT

Recoiling supermassive black holes (SMBHs) are considered one plausible physical mechanism to explain high velocity shifts between narrow and broad emission lines sometimes observed in quasar spectra. If the sphere of influence of the recoiling SMBH is such that only the accretion disc is bound, the dusty torus would be left behind, hence the SED should then present distinctive features (i.e. a mid-infrared deficit). Here, we present results from fitting the spectral energy distributions (SEDs) of 32 type-1 AGN with high velocity shifts between broad and narrow lines. The aim is to find peculiar properties in the multiwavelength SEDs of such objects by comparing their physical parameters (torus and disc luminosity, intrinsic reddening, and size of the 12 μm emitter) with those estimated from a control sample of ∼1000 *typical* quasars selected from the Sloan Digital Sky Survey in the same redshift range. We find that all sources, with the possible exception of J1154+0134, analysed here present a significant amount of 12 μm emission. This is in contrast with a scenario of an SMBH displaced from the centre of the galaxy, as expected for an undergoing recoil event.

Key words: methods: statistical – galaxies: active – galaxies: evolution – quasars: general.

1 INTRODUCTION

It is now widely accepted that galaxies host supermassive black holes (SMBHs) in their centre with masses of the order of 10^{6-9} $M_\odot$ (Salpeter 1964; Lynden-Bell 1969). Locally, the SMBH mass correlates with the mass (Magorrian et al. 1998; Marconi & Hunt 2003), with the velocity dispersion (Ferrarese & Merritt 2000; Tremaine et al. 2002), and with the luminosity of the host galaxy bulge (Kormendy & Richstone 1995). The existence of these correlations implies that the growth of the SMBH is tightly linked with the galaxy evolution, playing a crucial role in the SFH of the galaxy itself.

From the theoretical point of view, according to the hierarchical galaxy formation model, a main channel of galaxy growth is through mergers, that enhance star formation and trigger active galactic nuclei (AGN). Given that SMBH ubiquitously populate the centre of galaxies, it is expected that black hole binaries (BHBs) will be formed in the course of a merger event.

If the binary hypothesis is correct, BHB systems should leave characteristic features in the spectrum of the system such as a shift of the peak of their broad emission lines (BLs associated with the central BHs) with respect the narrow ones (NLs associated with the host galaxy; Begelman, Blandford & Rees 1980; Gaskell 1983). For example, objects showing *double-peaked emission* lines (DPEs) in their spectra might be interpreted as possible BHB candidates. Those systems present displaced broad-line peaks (one blueshifted and one redshifted compared with the narrow-line redshift) as a result of the orbital motion of the ionized gas gravitationally bound to the BH pairs. To date, long multi-epoch campaigns have ruled out the BHB interpretation for most of the DPEs studied (e.g. Eracleous & Halpern 1994). However, AGN showing single peaked shifted BLs are still considered plausible BHB candidates, as they

⋆ E-mail: lusso@mpia.de
† Hubble Fellow.

could be related to close binaries in which only one MBH is active (e.g. Bogdanović, Eracleous & Sigurdsson 2009; Dotti et al. 2009) and monitoring campaigns are ongoing to prove their nature (e.g. Eracleous et al. 2012; Decarli et al. 2013, hereafter Paper I; Ju et al. 2013; Liu et al. 2013).

Other alternative scenarios that might explain the BLs displacement are: (1) the projection of two unrelated quasars (QSOs) viewed, by chance, along similar sight lines, (2) a recoil induced by the anisotropic emission of gravitational waves in the final merge of SMBHs pairs (Peres 1962). The first interpretation relies on the probability of finding two unassociated quasars aligned with the line of sight. This turns out to be unlikely in several cases (see for example Boroson & Lauer 2009; Decarli, Reynolds & Dotti 2009). The latter is a prediction of general relativity, confirmed by numerical simulations, which imply that, after BHB coalescence, the resulting BH can recoil at velocities up to several thousand km s^{-1} due to anisotropic gravitational wave emission (e.g. Baker et al. 2007; Campanelli et al. 2007a, b; Lousto et al. 2012; Lousto & Zlochower 2013). Observationally, the recoiling SMBH and its surrounding gas would give rise to spectra where BLs are shifted from NLs of the host galaxy (e.g. Komossa, Zhou & Lu 2008; Comerford et al. 2009; Civano et al. 2010; Civano et al. 2012; Komossa 2012).

From a multiwavelength perspective, we expect the spectral energy distribution (SED) of DPEs or BHB candidates to have features similar to a 'typical' QSO SED: 'infrared bump' at ∼10 μm, and an upturn in the optical–UV, the so-called big-blue bump (BBB; Sanders et al. 1989; Elvis et al. 1994, 2012; Richards et al. 2006; Shang et al. 2011). The BBB is thought to be representative of the emission from the accretion disc around the SMBH, while the infrared bump is due to the presence of dust (from sub-parsec to hundreds parsec scale) which re-radiates a fraction of the optical–UV disc photons at infrared wavelengths.

The SED of a recoiling BH significantly displaced from the centre of the host galaxy might have instead different features. For example, if the sphere of influence of the recoiling BH on the gas were such that only the accretion disc is bound, all the larger scale structures (like a dusty torus) would be left behind, hence the SED should present the BBB only (Hao et al. 2010, hereafter H10; Guedes et al. 2011).

In this paper, we will present the broad-band SEDs, from ∼1500 Å to ∼20 μm, of a sample of 32 quasars identified by Tsalmantza et al. (2011). This sample has been selected from the Sloan Digital Sky Survey (SDSS; York et al. 2000) spectroscopic data base based on large velocity shifts (>1000 km s^{-1}) between NLs and BLs, and it spans the redshift range $0.136 \leq z \leq 0.713$. In Paper I, we presented their spectral properties (fluxes, line luminosities, widths, broad-line profiles and their evolution). Source are subsequently divided in four classes on the basis of the shape of the line profile: (1) fairly bell-shaped, strongly shifted BLs identify good BHB candidates; (2) BLs with tentative evidence of double-horned profiles are classified as DPEs; (3) objects with lines showing a rather symmetric base, centred at the redshift of the NLs, but an asymmetric core, resulting in a shifted peak, are called 'Asymmetric'; (4) other more complex profiles, or lines with relatively small shifts, or lines with asymmetric wings but modest peak shift are labelled as 'Others' (see fig. 2 in Paper I for examples of each class of objects). The main aim of the present analysis is to test whether the multiwavelength information can give further hints on the BHB scenarios described above. In order to quantify the contribution of host-galaxies and AGN reddening, as well as the disc and infrared AGN luminosities ($L_{\rm opt-UV}$ and $L_{\rm ir}$), we will make use of the SED-fitting code presented in Lusso et al. (2013).

We adopted a concordance Λcosmology with $H_0 = 70\,{\rm km\,s^{-1}\,Mpc^{-1}}$, $\Omega_{\rm M} = 0.3$, $\Omega_\Lambda = 1 - \Omega_{\rm M}$.

2 RECOILING SCENARIO

The SMBH ejected by gravitational wave recoil might carry along its accretion disc and broad-line region (BLR), but not the dusty torus (e.g. H10; Guedes et al. 2011), whose emission is peaked around 10–20 μm and is usually interpreted as hot-dust reprocessing of optical–UV radiation from the accretion disc. The temperatures involved are around 1000−1900 K depending on the different compositions of the dust grains,[1] which are located at scales that are dependent on the nuclear luminosity. In principle, the recoiling SMBH is able to drag along its surrounding dust only if its sphere of influence is larger than the torus size.

The SMBH sphere of influence is defined as the distance where the force on a test mass is dominated by the BH. The standard definition of sphere of influence is (see Merritt & Milosavljević 2005):

$$r_{\rm infl} = \frac{GM}{\sigma^2} \simeq 10.8\,{\rm pc} \left(\frac{M}{10^8\,{\rm M_\odot}}\right) \left(\frac{\sigma}{200\,{\rm km\,s^{-1}}}\right)^{-2}, \quad (1)$$

where M is the mass of the single BH formed via coalescence of two BHs, and σ is the 1D velocity dispersion of the stars in the nucleus. For a recoiling BH, $r_{\rm infl}$ needs to be scaled by the kick velocity $v_{\rm kick}$ such as

$$r_{\rm infl,recoil} \simeq 0.43\,{\rm pc} \left(\frac{M}{10^8\,{\rm M_\odot}}\right) \left(\frac{v_{\rm kick}}{1000\,{\rm km\,s^{-1}}}\right)^{-2}. \quad (2)$$

For a Milky Way BH mass of $4 \times 10^6\,{\rm M_\odot}$ and a kick velocity of 2000 km s^{-1} (e.g. Lousto et al. 2012) $r_{\rm infl,recoil}$ is extremely small ($\sim 4.3 \times 10^{-3}$ pc). Given that our sample consists of quasars, a more appropriate BH mass is of the order of $\sim 10^8\,{\rm M_\odot}$ (e.g. Komossa & Merritt 2008), which lead to a sphere of influence of 0.1 pc at the same kick velocity.

Tristram et al. (2009) found that the characteristic size of the 12 μm emitter scales approximately as the square root of the AGN luminosity

$$s_{12\,\mu{\rm m}} \cong 5.7 \times 10^{-22} \left(\frac{L_{12\,\mu{\rm m}}}{{\rm erg\,s^{-1}}}\right)^{0.5}\,{\rm pc}. \quad (3)$$

This relation has been estimated making use of high-resolution interferometric observations of nearby AGN with the MID-infrared Interferometric instrument at the Very Large Telescope Interferometer (see also Tristram & Schartmann 2011). The size of the 12 μm emitter vary from ∼0.6 pc at $L_{12\,\mu{\rm m}} \sim 10^{42}$ erg s^{-1}, to ∼20 pc at $L_{12\,\mu{\rm m}} \sim 10^{45}$ erg s^{-1}.

For a BH of $\sim 10^8\,{\rm M_\odot}$ and a typical 12 μm luminosity of $\sim 10^{45}$ erg s^{-1}, the torus size is ∼18 pc, hence the BH has no chance to carry along a significant amount of dust during the kick. The SED of such object would have a negligible or no infrared bump, or no 1 μm inflection. The disappearance of the torus emission once the BH is outside the torus region is extremely rapid, and can be roughly quantified as follows

$$\tau_{\rm dis} \cong \frac{R}{c} \cong 32.6 \frac{R}{10\,{\rm pc}}\quad {\rm yr}, \quad (4)$$

[1] The dust sublimation temperatures ranges around 1500–1900 K for graphite and 1000–1400 K for silicate grains (e.g. Laor & Draine 1993).

while the crossing time of a BH within a typical torus size (∼10 pc) is

$$\tau = \frac{R}{v_{\rm BH}} \cong 9.8 \times 10^4 \frac{R}{10\ {\rm pc}} \left(\frac{v_{\rm BH}}{1000\ {\rm km\ s^{-1}}}\right)^{-1} {\rm yr}. \quad (5)$$

These numbers reinforce the idea that the mid-infrared emission, once the BH is kicked, should become negligible on very short time-scales. Sources with low mid-infrared emission compared to the optical–UV one are known as *hot-dust-poor* AGN (HDP; H10, but see also Rowan-Robinson, Valtchanov & Nandra 2009; Jiang et al. 2010).

In the following, we will investigate if the QSOs presented in Paper I (which show large velocity shifts between NLs and BLs) may be interpreted in the context of the recoiling scenario through the analysis of their broad-band SEDs.

3 PHOTOMETRY

A well-sampled SED over a broad range of wavelength is mandatory in order to properly disentangle the emission associated with stellar light from that due to accretion and to constrain physical parameters from SED decomposition. We thus have collected the multiwavelength photometry from mid-infrared to optical–UV: *W*1, *W*2, *W*3 and *W*4 bands centred at wavelengths of 3.4, 4.6, 12 and 22 μm from the *Wide-field Infrared Survey Explorer* (*WISE*; Wright et al. 2010); *J*(1.25 μm), *H*(1.65 μm) and *K*(2.16 μm) bands from the *Two Micron All Sky Survey* (2MASS; Cutri et al. 2003); optical bands from the SDSS seventh data release (DR7; Abazajian et al. 2009); NUV(2306Å) and FUV(1551 Å) from the *Galaxy Evolution Explorer* (*GALEX*; Zamojski et al. 2007). The total number of employed bands is 14.

All QSOs are detected in *WISE* and SDSS, only three objects have not been detected in the 2MASS bands (J0927+2943, J0932+0318 and J1012+2613).

GALEX fluxes are collected from the online data base and images have been inspected visually. We have found that 28 objects have a *GALEX* detection and 7 out of these 28 sources have two observations from different surveys: all-sky imaging survey (AIS) and from the medium imaging survey (MIS). Three quasar (J0221+0101, J0829+2728 and J1440+3319) out of 7 show a difference between AIS and MIS photometry higher than 0.35 mag in both *GALEX* bands, which is a factor ∼2–3 difference in fluxes. For the SED fitting of J0221+0101, we use the flux measurements coming from the longest exposures (the MIS data). For J0829+2728, we consider the AIS fluxes because the values from the MIS were too faint to be consistent with the SDSS data (probably because this source was in the low state). For J1440+3319, we have found three observations from different surveys: AIS, nearby galaxy survey (NGS), and from a guest investigation (GI) programme. Fluxes for J1440+3319 vary by a factor of ∼2.7 in the NUV band from the AIS to the NGS survey (F_ν = 23.10–62.25 μJy, respectively). We have taken as reference flux value for this object the one from the GI programme, which is the deepest (see Appendix C for a more detailed discussion about the three varying objects). Overall, 21 objects[2] have data coming from MIS, 6 from AIS, and one from the GI programme; while for 4 objects we do not have any detection in both *GALEX* bands.

[2] J0918+3156 is detected only in the NUV band, while J0946+0139 has just an FUV detection from MIS. The latter is clearly visible in the NUV deep image, but it has been erroneously centred. The presence of a nearby galaxy might be the cause of the misalignment. For this source, we have decided to consider the data coming from the AIS survey.

4 MODEL FITTING

The SED-fitting code utilized in this paper is the one already presented in Lusso et al. (2013, hereafter L13). The various components (i.e. hot-dust from a dusty torus, host galaxy and accretion disc emission) of the rest-frame SEDs are fitted by using a standard χ^2 minimization procedure (see section 3 in L13 for details about the model fitting). The code is based on a large set of templates widely used in the literature. Details about the SED decomposition procedure are given in Appendix A.

The infrared luminosity $L_{\rm ir}$ and the accretion disc luminosity $L_{\rm opt-UV}$ are obtained by integrating the torus template between 1 and 1000 μm, and the disc template between 1 and 0.003 μm (i.e. the last point of the BBB template; Richards et al. 2006), respectively.

Infrared luminosities need to be corrected for the anisotropy factor defined as the ratio of the luminosity of face-on versus edge-on AGN, which is a function of the column density $N_{\rm H}$ (Pozzi et al. 2007). This correction is negligible for QSOs fitted with a torus template having $N_{\rm H}$ lower than 10^{22} cm^{-2} (72 per cent of the total sample). Nine objects have best-fitting torus with $10^{22} < N_{\rm H}\,[{\rm cm^{-2}}] < 10^{23}$. The anisotropy correction for these sources is at any rate modest, of the order of 1.3 (Pozzi et al. 2007; Vasudevan et al. 2010; Lusso et al. 2011, 2012).

We point out that *WISE* bands might be contaminated by emission features due to the stochastic heating of polycyclic aromatic hydrocarbon (PAH) molecules or carbon grains (e.g. Flagey et al. 2006), which are related with massive star-forming regions at much lower dust temperature ($T < 100$ K). However, PAH features are almost absent in AGN, given that these molecules are destroyed by the extreme optical–UV and soft X-ray radiation in AGN (Roche et al. 1991; Siebenmorgen, Krügel & Spoon 2004). Therefore, on average our estimates of the infrared 'torus' luminosities are mainly dominated by the AGN emission.

Intrinsic disc luminosities are estimated by de-reddening the BBB template according to the assumed reddening law, and employing the reddening value related with the BBB template found as the best solution.

5 PROPERTIES OF THE SEDS

In Fig. 1, we present the best-fitting decomposition for each object in our sample. In order to further test our fits, we have compared the best-fitting templates with the optical spectra from SDSS (grey line in Fig. 1). Note that spectra are not renormalized to match the SDSS photometry and they are not corrected for aperture. Overall, optical spectra are in good agreement with the results from the model fitting procedure. In general, our model fitting shows that almost all QSO SEDs are contaminated by host galaxy emission around 1 μm and/or reddening in the optical–UV.

In order to distinguish among galaxy-dominated, QSO-dominated and reddening-dominated SEDs, we have considered the mixing diagram presented by Hao et al. (2013). The mixing diagram axes are the 1–3 μm SED slope ($\alpha_{\rm NIR}$) versus the 0.3–1 μm slope ($\alpha_{\rm OPT}$). These ranges lie on either side of the 1 μm dip of the rest-frame SED. Fig. 2 shows the mixing diagram our QSO sample. The slopes $\alpha_{\rm NIR}$ and $\alpha_{\rm OPT}$ are estimated from the best-fitting SED (red line in Fig. 1). Different regions of the plot correspond to different SED shapes, as shown by the black lines in the four corners of the plot. Galaxy SEDs lie in the top-left corner in this diagram. As soon as the galaxy contribution decreases, objects move along the blue tracks further down to the QSO-dominated region (bottom-left

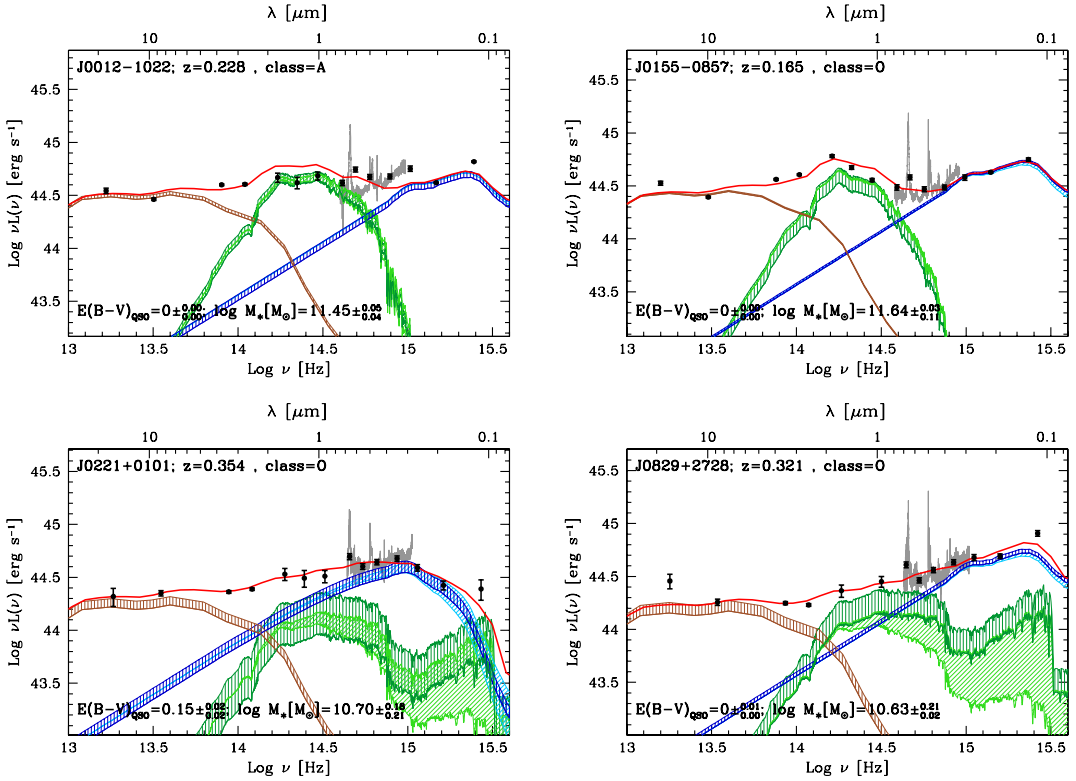

Figure 1. Rest-frame SED decompositions of the quasars sample. Each panel shows source's name, redshift, class, best-fitting AGN reddening (estimated considering the Prevot et al. 1984 reddening law), and best-fitting stellar mass with uncertainties. Object classification is based on the shape of Balmer lines: B – BHB candidates; D - DPEs; A – sources with Asymmetric line profiles; O – others. Black circles are the observed photometry in the rest-frame (from infrared to optical-UV). The brown, dark green and blue dashed regions correspond to the uncertainties (see Section 4) on the normalization of the hot-dust from reprocessed AGN emission, galaxy and BBB templates, respectively. The light green and cyan dashed regions encompass the uncertainty on the BBB and galaxy reddening, respectively. The red line represents the best-fitting SED. Grey line shows the optical spectrum from SDSS.

corner). HDP QSOs and are located in the top-right region of the mixing diagram.

Overall, the sample shows a large SED variety with moderately host galaxy contamination and extinction. There is no clear division among different classes, but SEDs of BHB candidates and DPEs lie along the QSO–host galaxy tracks, with modest intrinsic reddening, in agreement with the bulk of the population in SDSS. Objects classified as 'asymmetric' and most of the 'others' cover a wider range of host galaxy and intrinsic reddening contamination. A summary of the general properties our quasar sample is given in Table 1. The disc luminosities reported in Table 1 have been de-reddened considering the best-fitting $E(B-V)_{\rm qso}$ and the Prevot et al. (1984) reddening law. Details on the SED general properties for the different classes are given in Appendix B.

6 HDP CANDIDATES

Almost all objects in our sample show emission from warm/hot dust which is a clear indication of optical–UV AGN luminosity reprocessed by a dusty torus. An HDP quasar should have small mid-infrared to disc luminosity ratios ($R = L_{\rm ir}/L_{\rm opt-UV}$).[3]

[3] R should be defined as the mid-infrared to bolometric luminosity ratio, where the bolometric luminosity is estimated in the optical–UV/X-ray wavelength range. X-ray data are not available for the majority of the sources in our sample, hence are not considered in the present analysis. Since the X-ray emission is of the order of ∼10–20 per cent of the bolometric budget, the R values may be overestimated by a similar factor.

Following Hao et al. (2011), HDP quasars should have R values between ∼2 per cent to 30 per cent, well below the 75 per cent predicted by the unified model.

We have thus considered, for the following analysis, the R values where the $L_{\rm opt-UV}$ estimates are corrected for both host galaxy contamination and disc reddening, and in order to classify a quasar HDP, we have searched for those objects with low mid-infrared to disc luminosity ratios.

Only one source, J1154+0134 (class = BA) shows significantly lower hot dust luminosity compared with what expected from its optical–UV emission, by about one order of magnitude assuming an average R of 0.3−0.6 (e.g. Treister, Krolik & Dullemond 2008; Ma & Wang 2013; L13). According to the position of J1154+0134 relative to the equal slope in the $\alpha_{\rm OPT}-\alpha_{\rm NIR}$ plot, the infrared emission should be the continuation of the disc emission to longer wavelengths (2−3 μm, see Hao et al. 2013.). The flattening of the $W3$ and $W4$ bands at $\lambda > 7$ μm indicates still little mid-infrared emission. The R values of J1154+0134 is 0.07 considering the de-reddened $L_{\rm opt-UV}$ and 0.27 if we use the reddened $L_{\rm opt-UV}$ value, which are consistent with the expected R values for class II HDP[4] estimated by H10. Assuming a conservative error on R of the order of 5 per cent (see L13), the difference between the value predicted by unified models and the one of J1154+0134 is significant at 6.5σ level (for $R = 0.27$).

[4] Class I, II and III HDP are sources lying below, on and above the equal slope line in the mixing diagram, respectively (see section 2 by H10).

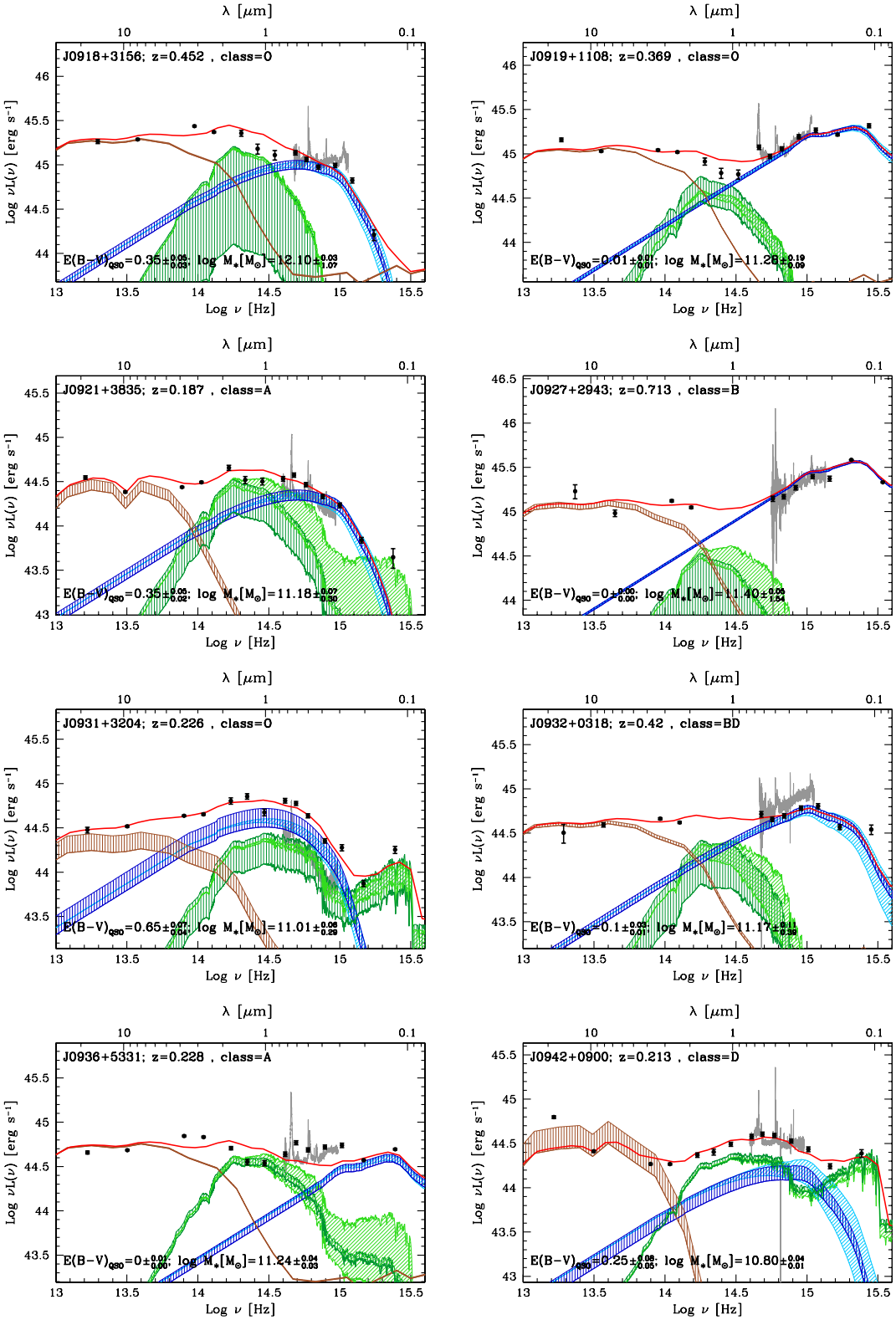

Figure 1 – *continued*

In conclusion, all quasars in our sample (aside from J1154+0134) show mid-infrared emission, and therefore, it is unlikely that our objects have experienced a recoil event (in a scenario of a single BH displaced from the centre of the galaxy).

6.1 The case of J1154+0134

J1154+0134 has been newly selected as BHB candidate by both Tsalmantza et al. (2011) and Eracleous et al. (2012). The optical spectrum of this object and the evolution of the broad-line profiles

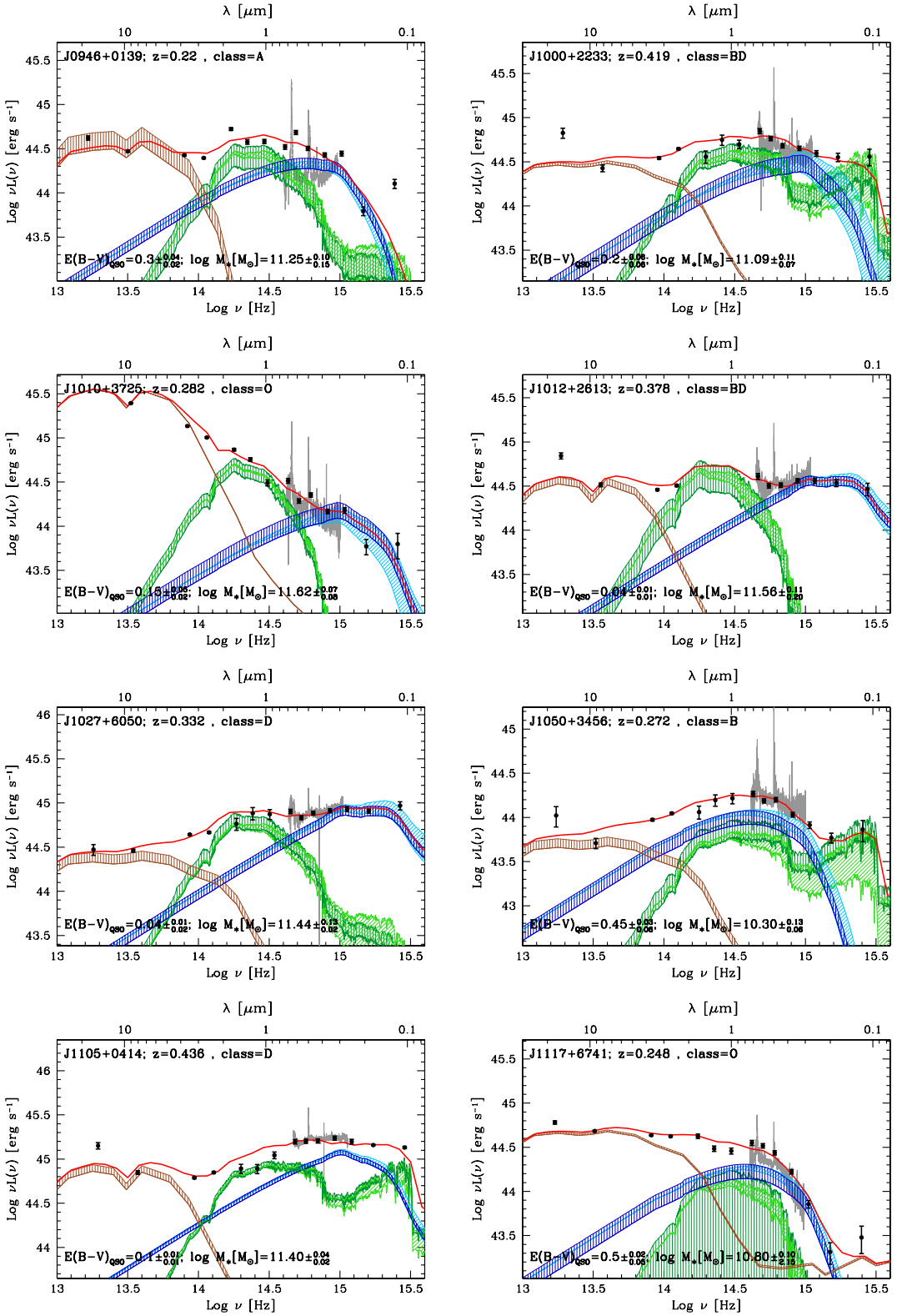

Figure 1 – *continued*

are discussed in Paper I (see also Eracleous et al. 2012). From the spectral point of view, this source presents Hβ and Mg II lines with similar profiles, blueshifted peaks ($\sim$3500 km s^{-1}), red asymmetries and do not show any significant evolution of the shift of broad-line peaks between the SDSS spectrum and our follow-up observations.

J1154+0134 has been also targeted with the Cosmic Origins Spectrograph (COS) on the *Hubble space Telescope* (*HST*) in 2011 May with the grating NUV/G230L (central wavelength 2950 Å, covering the windows 1649–2051 Å and 2749–3151 Å) to observed the Lyα line (see Fig. 3). The line shows blue asymmetries with the peak of

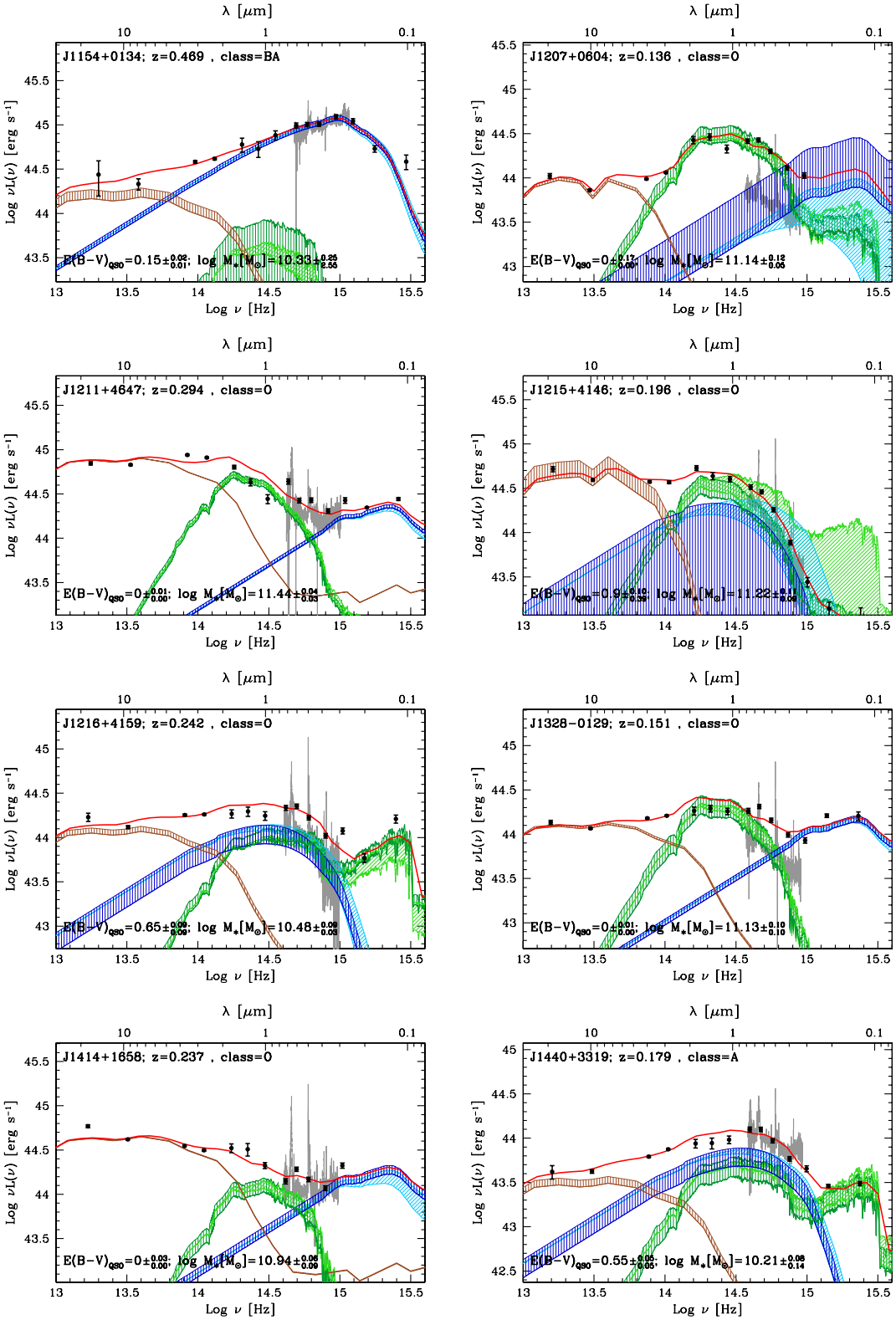

Figure 1 – *continued*

Lyα consistent with the redshift from narrow lines. This spectrum has low signal-to-noise ratio and no other lines are present. The UV observation hints at a DPE nature of J1154+0134, but more detailed analysis and discussion of the UV spectrum will be given in Eracleous et al. 2014.

J1154+0134 is not detected by *ROSAT*, but it is clearly detected in the Faint Images of the Radio Sky at Twenty cm (Becker, White & Helfand 1995) survey with a measured peak flux density of 1.54 mJy. If J1154+0134 is a recoiling SMBH, high-resolution radio and *HST* observations would provide precise measurement of its location.

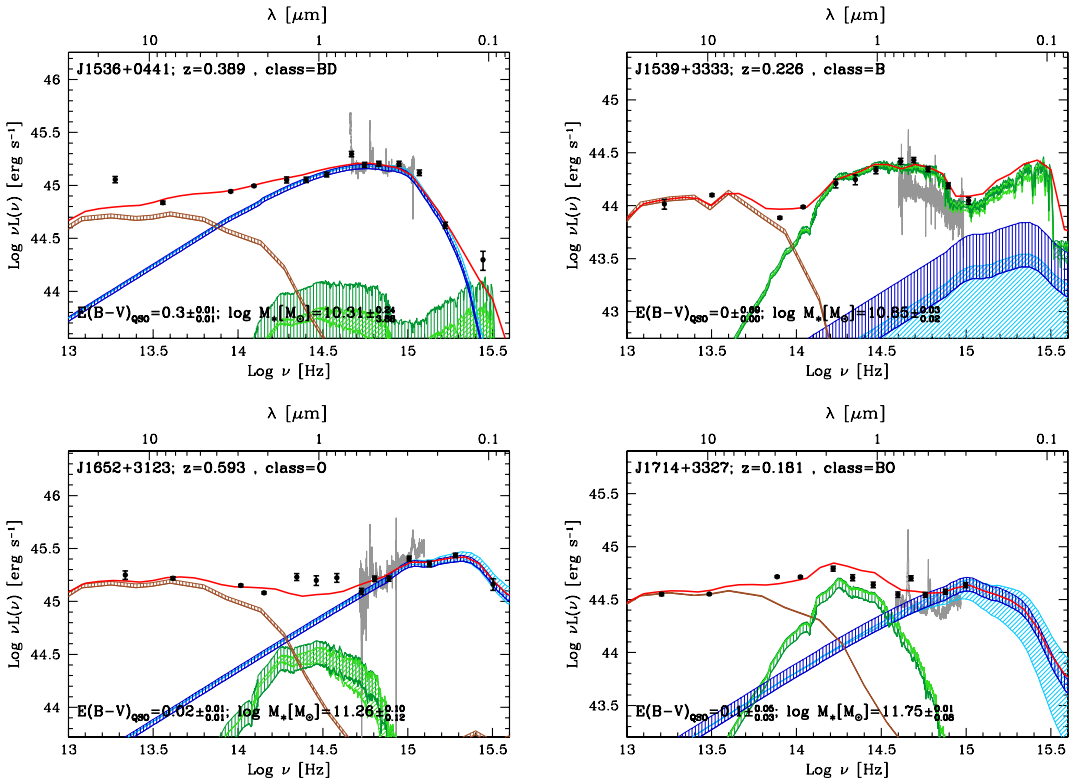

Figure 1 – *continued*

7 X-RAY DETECTION

In the last decade several authors (e.g. Lodato et al. 2009; Sesana et al. 2012; Gültekin & Miller 2012; Tanaka, Menou & Haiman 2012, and references therein) have modelled the observable signatures related to annular gaps or larger central cavities in the accretion disc around an SMBH caused by the presence of secondary BH orbiting in a binary system. The SED of such systems is predicted to show standard emission in the optical bands with a peculiar dimming in the UV and possibly in the X-rays, depending on the gap extent and the amount of material present in this region. In order to observe a decrease in the disc emission at UV or at shorter wavelength, the binary separations (a) considered in these works are $a \leq 0.01$ pc for BH masses of 10^8-10^9 $M_\odot$. The peculiar AGN targeted in our analysis are characterized by the presence of displaced BLs that in the binary scenario are associated with the BLR bound to the single accreting BHs. Consistently the binary separations have to be $a \geq R_{\rm BLR}$. Taking into account the range of optical luminosities computed for our targets $a \geq 0.1$ pc (Bentz et al. 2013). Hence, we do not expect our objects to be unusually under luminous in the UV/X-rays. However, due to the large uncertainties in the theoretical modelling and the complete lack of observations of accreting sub-pc BHBs, we decided to check also the X-ray properties of our objects. We found 11 objects serendipitously detected in the ROSAT All-Sky Survey (RASS), while 2 sources have *ROSAT* high resolution imager (HRI) observations. The X-ray fluxes at 0.5–2 keV were calculated from the count rates in the *ROSAT* band (0.1–2.4 keV) by employing a power-law spectrum with no intrinsic absorption and a photon index $\Gamma = 2.0$ modified by Galactic absorption (Kalberla et al. 2005). Table 2 lists the X-ray properties of the detected RASS objects in our sample. Among these 13 quasars, two have additional spectral information from *XMM–Newton* (J0155−0857) and *Chandra* (J0927+2943).

J0155−0857 was also found serendipitously in an *XMM–Newton* observation (nominal exposure time of ∼13 ks) in 2007 June. Although the observation shows a high level of background, the source is bright enough to allow an X-ray spectral analysis. A total of ∼2000/1500/1300 source net counts were collected in the pn/mos1/mos2 (0.3–7 keV band) using circular extraction regions of radius 30/25/20 arcsec, respectively. Since the source is located partly on a CCD gap in the pn camera, we focused our attention to the mos1 and mos2 spectral data. A power law with photon index $\Gamma = 1.94 \pm 0.06$ provides a good fit to the data, with no apparent need for additional spectral components. This is confirmed by the pn data. The observed 0.5–2 keV flux is $\sim 7.0 \times 10^{-13}$ erg s^{-1} cm^{-2}, consistent with the *ROSAT* observation.

J0927+2943 was targeted by *Chandra* with the Advanced CCD Imaging Spectrometer (ACIS-S) in 2009 February; the nominal exposure of 26.7 ks provided ∼60 net counts in the 0.5–7 keV band. The spectrum is fitted with a power law of $\Gamma = 0.1$, which is unusual for AGN, suggesting a significant level of obscuration. In this case, assuming a more canonical photon index of 1.8, we obtain $N_{\rm H} = 7.7(+8.4-5.1) \times 10^{22}$ cm^{-2}. The observed flux in the 0.5–2 keV band (adopting the fitted Γ) is 3.6×10^{-15} erg s^{-1} cm^{-2}, much lower than the one obtained from the *ROSAT* observation. Long-term X-ray variability may be responsible for the observed difference in the X-ray flux.

J1328−0129 has not been detected by *ROSAT*, but was serendipitously observed by *Chandra* with ACIS-I in 2012 August, with a nominal exposure of 5 ks; the number of source net counts in the 0.5–7 keV bad is ∼830. The spectrum is fitted with a power law of $\Gamma = 1.2 \pm 0.1$, which may suggest some level of obscuration. Fitting the data with a power law with $\Gamma = 1.8$ (i.e. typical for AGN emission) modified by absorption, we obtain $N_{\rm H} = 5.5(+1.2-1.1) \times 10^{21}$ cm^{-2}. The observed flux in the 0.5–2 keV band is 5.3×10^{-13} erg s^{-1} cm^{-2}.

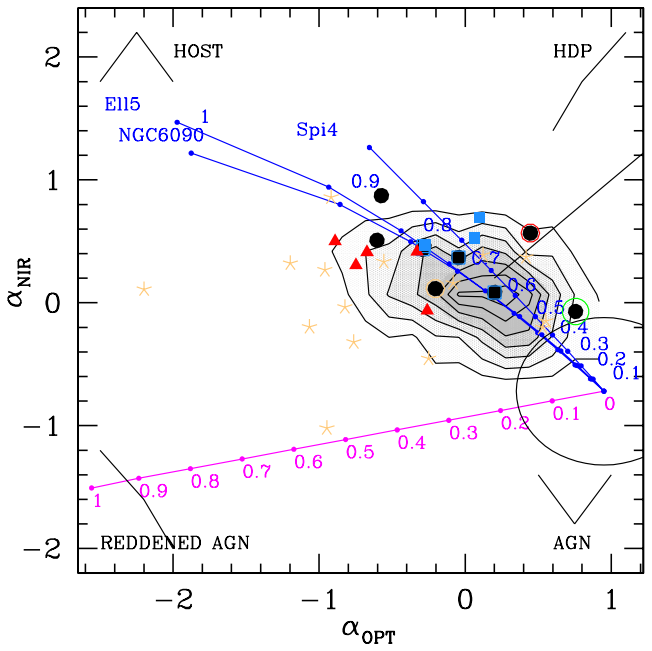

Figure 2. The mixing diagram of the quasar sample. Different regions of the plot correspond to different SED shapes, as shown by the black lines in the four corners of the plot. The black circle shows the 1σ dispersion of the quasar samples of E94 as defined by Hao et al. (2013). The blue tracks show composite QSO+host galaxy templates for three different host galaxy types (Polletta et al. 2007), while the numbers beside these curves represent the galaxy fraction. As QSO template, we refer here to the mean SED by E94. The purple track shows the reddening vector applied to the E94 radio-quiet mean SED. The numbers under the reddening vector show the $E(B-V)_{qso}$ values. The straight black solid line shows the $\alpha_{OPT} = \alpha_{NIR}$ line. Points are the sources from Tsalmantza et al. (2011) coded on the basis of the shape of Balmer lines: B – BHB candidates (black filled circles); D – DPEs (blue filled squares); A – sources with asymmetric line profiles (red filled triangles); O – others (orange stars). BHB candidates where the classification scheme is not univocal are marked with an additional symbol: BD – BHB/DPEs candidates (blue open squares); BA – BHB/asymmetric (red open circle); BO – BHB/other (orange open circle). The green circle marks the recoil BH candidate J0927+2943 (Komossa et al. 2008). We overplot the contours for the test sample of about 1000 QSOs in SDSS (see Section 8.1).

Among the detected objects, all soft luminosities are, on average, typical of bright AGN/quasars (aside from the *Chandra* observation of J0927+2943).

Sources without a *ROSAT* detection might be either intrinsically faint, X-ray obscured and/or highly variable. Bolometric luminosities of the detected objects are, on average, brighter than the undetected ones, as expected. Given that the X-ray luminosity scales with the bolometric luminosity by a factor of about 30 for optically selected QSO (Marconi et al. 2004), we expect the undetected AGN to have X-ray luminosities of the order of 10^{43} erg s^{-1} or lower.[5] Deep X-ray observations with *Chandra* and *XMM–Newton* are needed in order to establish if undetected RASS objects are intrinsically faint or X-ray obscured.

[5] The *ROSAT* flux limit is 5×10^{-13} erg s^{-1} cm^{-2} for a mean effective exposure time of 400 s, but the range of *ROSAT* exposure times is large, and the sensitivity limit is different from field to field (Voges et al. 1999).

8 ADDITIONAL PROPERTIES

8.1 Comparison with a test sample

Are the SEDs of quasars with spectra showing high velocity shifts between broad and narrow lines peculiar with respect to *typical* QSOs? To answer this question we have selected an appropriate control sample of type-1 QSOs from the one described by Krawczyk et al. (2013, hereafter K13). The main sample in K13 contains 119 652 QSOs from both SDSS-DR7 (103 895 objects with $i < 19.1$ for $z < 3$ and $i < 20.2$ for $z > 3$) and the Two Degree Filed QSO Redshift survey (15 757 with $b_J < 20.85$ for $z < 3$; Croom et al. 2004) with $0.064 < z < 5.46$. Mid-IR photometry is coming from *Spitzer* and *WISE*, near-infrared data from 2MASS and UKIDSS, optical data from SDSS, and UV data from *GALEX*.

From the K13 sample, we have selected all objects with the same redshift range as the one explored in the present analysis (17 666 objects with $0.136 \leq z \leq 0.713$). Well-constrained L_{ir} measurements require a detection at $\sim$10 μm, we thus considered a sub-sample of sources detected in *W4* (i.e. the *W4* band is redshifted at $\sim$13 μm for our maximum redshift of 0.713), bringing the final sample size to 13 634 QSOs. The redshift distribution of this sample is very different than the one covered by our quasars. The median redshift of the typical QSO sample is 0.474, while the median redshift of our sample is 0.272. We have thus further cut the sample of typical QSOs by extracting at random $\sim$1000 objects following the redshift distribution of our sample. A Kolmogorov–Smirnov (K–S) test confirms that the two redshift distributions are drawn from the same parent population (see Table 3). We then run our SED-fitting code on this control sample and we estimate intrinsic reddening, torus and disc luminosities for all objects.

8.2 Intrinsic reddening distribution

Fig. 4 shows a comparison of the disc reddening distribution between our sample and the control sample. On average, our sample presents a higher level of intrinsic obscuration with respect to the match sample. The mean disc reddening for our sample is $\langle E(B-V)_{qso}\rangle \simeq 0.20$ with a standard dispersion of 0.24 (the median $E(B-V)_{qso}$ is 0.1 with 16th and the 84th percentile at 0 and 0.45, respectively), while the control sample has $\langle E(B-V)_{qso}\rangle \simeq 0.08$ with $\sigma = 0.14$ (median $\langle E(B-V)_{qso}\rangle \simeq 0.03$ with 16th and the 84th percentile at 0 and 0.15, respectively). A K–S test rules out the hypothesis that the two samples have, on average, similar $E(B-V)_{qso}$ values. However, the difference in the reddening distributions is mainly dominated by 'others' and 'asymmetric', and it is no longer statistically significant (1.4σ level) when we restrict to the objects classified as BHB candidates (nine sources classified as B, BD, BO and BA). The AGN reddening value for each object is listed in Table 1, while Table 4 contains the average reddening values for each class.

8.3 Luminosity distributions

We have further checked if the control and our sample are probing different luminosities in the same redshift bin. In the top panel of Fig. 5, we present a comparison of the best-fitting disc luminosities between the control and our sample. These luminosities are host galaxy subtracted but with disc reddening left in. The mean disc luminosity for our sample is $\langle \log L_{opt-UV}\rangle \simeq 44.77$ (in erg s^{-1}) with a standard dispersion of 0.53 (the median $\log L_{opt-UV}$ is 44.79), while the control sample has a mean of 44.75 with

Table 1. General properties of our quasar sample.

Obj.name[a]	$z^b_{\rm NL}$	$\alpha^c_{\rm OPT}$	$\alpha^d_{\rm NIR}$	$\log L^e_{\rm ir}$	$\log L^f_{\rm opt-UV,dered}$	$\log L^g_{\rm opt-UV,red}$	$E(B-V)^h_{\rm qso}$	$\log L^i_{12\,\mu\rm m}$	$s^j_{12\,\mu\rm m}$	Class[k]	$\log M^l_*$
J0012−1022	0.228	−0.33	0.42	44.97	45.05	45.05	$0.00^{+0.00}_{-0.00}$	44.48	9.95	A	$11.45^{+0.05}_{-0.04}$
J0155−0857	0.165	−0.08	0.16	44.89	45.05	45.05	$0.00^{+0.00}_{-0.00}$	44.41	9.09	O	$11.64^{+0.03}_{-0.11}$
J0221+0101	0.354	0.12	0.39	44.75	45.38	44.79	$0.15^{+0.02}_{-0.02}$	44.26	7.71	O	$10.70^{+0.18}_{-0.21}$
J0829+2728	0.321	0.42	0.37	44.68	45.05	45.05	$0.00^{+0.01}_{-0.00}$	44.19	7.12	O	$10.63^{+0.21}_{-0.02}$
J0918+3156	0.452	−0.82	−0.03	45.74	46.10	45.14	$0.35^{+0.05}_{-0.03}$	45.25	24.05	O	$12.10^{+0.03}_{-1.07}$
J0919+1108	0.369	0.53	−0.20	45.51	45.68	45.62	$0.01^{+0.01}_{-0.01}$	45.02	18.49	O	$11.28^{+0.19}_{-0.09}$
J0921+3835	0.187	−0.75	0.31	44.96	45.45	44.49	$0.35^{+0.05}_{-0.02}$	44.48	9.91	A	$11.18^{+0.07}_{-0.30}$
J0927+2943	0.713	0.76	−0.07	45.54	45.89	45.89	$0.00^{+0.00}_{-0.00}$	45.05	19.07	B	$11.40^{+0.05}_{-1.54}$
J0931+3204	0.226	−1.20	0.32	44.88	45.86	44.54	$0.65^{+0.07}_{-0.04}$	44.40	8.99	O	$11.01^{+0.06}_{-0.29}$
J0932+0318	0.420	0.20	0.08	45.06	45.45	45.00	$0.10^{+0.03}_{-0.01}$	44.57	11.03	BD	$11.17^{+0.11}_{-0.39}$
J0936+5331	0.228	−0.26	−0.06	45.20	44.95	44.95	$0.00^{+0.01}_{-0.00}$	44.71	12.97	A	$11.24^{+0.04}_{-0.03}$
J0942+0900	0.213	−0.28	0.47	44.91	45.21	44.42	$0.25^{+0.08}_{-0.05}$	44.46	9.64	D	$10.81^{+0.04}_{-0.01}$
J0946+0139	0.220	−0.67	0.41	44.97	45.39	44.50	$0.30^{+0.04}_{-0.02}$	44.51	10.26	A	$11.25^{+0.10}_{-0.15}$
J1000+2233	0.419	−0.28	0.46	44.94	45.39	44.69	$0.20^{+0.06}_{-0.06}$	44.45	9.62	BD	$11.09^{+0.11}_{-0.07}$
J1010+3725	0.282	−0.95	−1.02	45.99	44.94	44.35	$0.15^{+0.05}_{-0.02}$	45.51	32.48	O	$11.62^{+0.07}_{-0.08}$
J1012+2613	0.378	−0.29	0.44	45.04	45.11	44.90	$0.04^{+0.01}_{-0.01}$	44.56	10.82	BD	$11.56^{+0.11}_{-0.20}$
J1027+6050	0.332	0.06	0.53	44.88	45.47	45.25	$0.04^{+0.01}_{-0.02}$	44.40	8.98	D	$11.44^{+0.13}_{-0.02}$
J1050+3456	0.272	−0.60	0.51	44.19	45.22	44.12	$0.45^{+0.03}_{-0.06}$	43.70	4.04	B	$10.30^{+0.13}_{-0.06}$
J1105+0414	0.436	0.10	0.69	45.37	45.76	45.31	$0.10^{+0.01}_{-0.01}$	44.89	15.94	D	$11.40^{+0.04}_{-0.02}$
J1117+6741	0.248	−1.07	−0.20	45.13	45.46	44.30	$0.50^{+0.02}_{-0.05}$	44.64	11.94	O	$10.80^{+0.10}_{-2.15}$
J1154+0134	0.469	0.45	0.57	44.71	45.87	45.28	$0.15^{+0.02}_{-0.01}$	44.22	7.35	BA	$10.33^{+0.25}_{-2.55}$
J1207+0604	0.136	−0.92	0.86	44.44	44.32	44.32	$0.00^{+0.17}_{-0.00}$	43.96	5.46	O	$11.14^{+0.12}_{-0.05}$
J1211+4647	0.294	−0.76	−0.32	45.35	44.68	44.68	$0.00^{+0.01}_{-0.00}$	44.86	15.33	O	$11.44^{+0.04}_{-0.03}$
J1215+4146	0.196	−2.20	0.11	45.10	45.58	44.03	$0.90^{+0.10}_{-0.39}$	44.64	11.95	O	$11.22^{+0.11}_{-0.09}$
J1216+4159	0.242	−0.96	0.27	44.56	45.38	44.06	$0.65^{+0.09}_{-0.09}$	44.07	6.16	O	$10.48^{+0.09}_{-0.03}$
J1328−0129	0.151	−0.56	0.33	44.56	44.51	44.51	$0.00^{+0.01}_{-0.00}$	44.07	6.17	O	$11.13^{+0.10}_{-0.10}$
J1414+1658	0.237	−0.25	−0.45	45.10	44.60	44.60	$0.00^{+0.03}_{-0.00}$	44.61	11.51	O	$10.94^{+0.06}_{-0.09}$
J1440+3319	0.179	−0.89	0.50	43.99	45.07	43.86	$0.55^{+0.05}_{-0.05}$	43.50	3.21	A	$10.21^{+0.08}_{-0.14}$
J1536+0441	0.389	−0.04	0.37	45.18	46.23	45.35	$0.30^{+0.01}_{-0.01}$	44.69	12.68	BD	$10.31^{+0.24}_{-3.88}$
J1539+3333	0.226	−0.57	0.87	44.53	43.87	43.87	$0.00^{+0.69}_{-0.00}$	44.08	6.21	B	$10.85^{+0.03}_{-0.02}$
J1652+3123	0.593	0.55	−0.15	45.65	45.86	45.74	$0.02^{+0.01}_{-0.01}$	45.16	21.69	O	$11.26^{+0.10}_{-0.12}$
J1714+3327	0.181	−0.20	0.12	45.03	45.31	44.86	$0.10^{+0.05}_{-0.03}$	44.54	10.63	BO	$11.75^{+0.01}_{-0.08}$

Note. [a]Quasar name.
[b]Redshift of narrow lines.
[c]Optical slope estimated from the best-fit SED in the wavelength range 0.3−1 μm.
[d]Near-infrared slope estimated from the best-fitting SED in the wavelength range 1−3 μm.
[e]Logarithm of the infrared luminosity (in erg s^{-1}) integrated from the best-fitting torus template between 1 and 1000 μm.
[f]Logarithm of the de-reddened disc luminosity (in erg s^{-1}) integrated from the best-fitting BBB template from 1 μm to $\log\nu = 17$ (in Hz).
[g]Logarithm of the reddened disc luminosity (in erg s^{-1}) integrated from the best-fitting BBB template from 1 μm to $\log\nu = 17$ (in Hz).
[h]Best-fitting AGN reddening value.
i Logarithm of the 12 μm luminosity (in erg s^{-1}) estimated from the best-fitting torus template.
[j]The approximate size of the emitter (in pc) at 12 μm from equation (3).
[k]Object classification based on the shape of the Balmer lines: B – BHB candidates; D – DPEs; A – sources with asymmetric line profiles; O – others. The classification scheme is not univocal and different classes are not mutually exclusive (e.g. BHB candidates may have spectral feature similar to the DPEs, see Paper I for details): BD – BHB/DPEs candidates; BA – BHB/Asymmetric; BO – BHB/other.
[l]Best-fitting stellar mass (in $M_\odot$) from BC03 model using a Chabrier IMF.

$\sigma = 0.48$ (median $\langle \log L_{\rm opt-UV} \rangle \simeq 44.74$). The two distributions are found to be consistent, as verified via a K–S test.

We have also computed the host-galaxy luminosity ($L_{\rm host}$) from the best-fitting galaxy template for each quasar in our sample and in the control sample over the same wavelength range of $L_{\rm opt-UV}$. We found that the ratio between $L_{\rm host}$ and $L_{\rm opt-UV}$ is more than 0.7 for ∼31 per cent of the quasars in our sample, while for the control sample is about 10 per cent. This means that the host galaxy is generally brighter in our sample for a given $L_{\rm opt-UV}$. For these objects the host galaxy fraction might be considered an upper limit given that the best-fitting host galaxy solution is degenerate with their reddened BBB as shown in Fig. 1 (the shaded areas correspond to the higher and lower uncertainty in the normalization). In fact, the shape of a highly reddened BBB is similar to the one of the galaxy

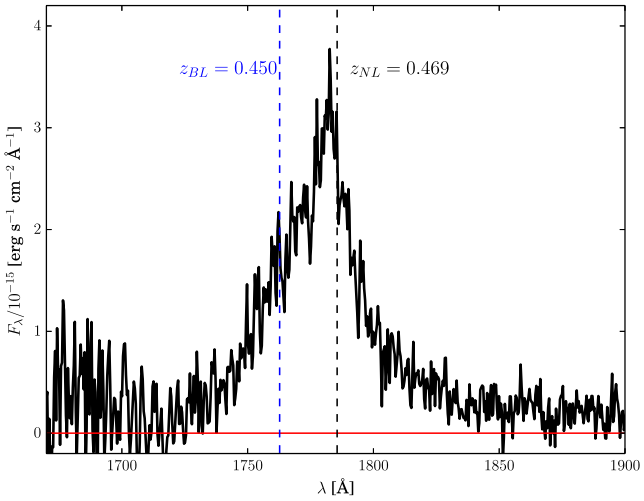

Figure 3. *HST*/COS ultraviolet spectrum of J1154+0134 displaying Lyα emission. The red solid line denotes the zero level, while the two vertical dashed lines mark the broad-line (blue) and narrow-line (black) redshift.

and therefore the finding of higher host galaxy contamination in our sample than in the control sample might be simply biased by the reddening distribution. Further details on the SED fits for these 10 objects are given in Appendix C.

Given that our sample have the tendency to be more reddened than the control sample, once we have corrected for the intrinsic $E(B-V)_{\rm qso}$, the disc luminosities in the BHB sample are actually higher than the ones in the control sample. In the bottom panel of Fig. 5a comparison of the intrinsic disc luminosities (host galaxy subtracted and corrected for reddening) for the two samples is presented. It is apparent that after applying the reddening correction, the disc luminosities of our sample are, on average, higher than the one in the control sample. The mean disc luminosity for our sample is $\langle \log L_{\rm opt-UV} \rangle \simeq 45.30$ (in erg s^{-1}) with a standard dispersion of 0.52 (the median $\log L_{\rm opt-UV}$ is 45.38), while the control sample has a mean of 45.03 with $\sigma = 0.38$ (median $\langle \log L_{\rm opt-UV} \rangle \simeq 45.02$). If we perform again a K–S test, we rule out the hypothesis that the two samples have similar means.

We further tested whether the difference in the average reddening values between our sample and the control may be explained by the small sample differences in luminosity. Fig. 6 shows $L_{\rm ir}$ as a function of $L_{\rm opt-UV,red}$ for our sample and the control objects. We have then selected a region in this plot where our sample and the control one have similar $L_{\rm ir}$ and $L_{\rm opt-UV,red}$ values. The red dashed lines encompass the region where the average values for $L_{\rm ir}$ and $L_{\rm opt-UV,red}$ are similar within $\sim 1.6\sigma$. The average values for $L_{\rm ir}$, $L_{\rm opt-UV,red}$ and $E(B-V)_{\rm qso}$ are reported in Table 5. We find that there is no significant difference (1.7σ level) between the mean reddening values in the two samples at matched $L_{\rm ir}$ and $L_{\rm opt-UV,red}$, although we note that the $L_{\rm ir}$ and $L_{\rm opt-UV,red}$ intervals are quite narrow.

In summary, the SEDs of our sample are, on average, (1) characterized by moderately higher reddening values than the ones estimated in a control sample of typical QSOs, and (2) the host galaxy contamination is higher in our sample than in the control sample. The latter result might be due to degeneracies between host galaxy

Table 3. Kolmogorov–Smirnov test and their significance from *t*-Student test to determine if our sample (32 objects) and the control sample (∼1000 objects) are significantly different for a given parameter of interest.

Parameter[a]	K–S[b]	*t*-Student (σ)
z	$D = 0.12$ with prob $= 0.72$	0.25
$E(B-V)_{\rm qso}$	$D = 0.30$ with prob $= 5.0 \times 10^{-3}$	2.70
$L_{\rm opt-UV,red}$	$D = 0.10$ with prob $= 0.88$	0.21
$L_{\rm opt-UV,dered}$	$D = 0.37$ with prob $= 2.5 \times 10^{-4}$	3.00
$s_{12\,\mu\rm m}$	$D = 0.32$ with prob $= 2.7 \times 10^{-3}$	2.20

Note. [a]Parameter of interest in the comparison of our sample with the control sample.
[b]Kolmogorov–Smirnov test and two-sided probability that the two samples are drawn from the same parent population.

Table 2. RASS properties of our quasar sample.

Obj. name[a]	Count rate[b] (s^{-1})	Exposure[c] (s)	$N_{\rm H}$[d] (cm^{-2})	$F_{[0.5-2]\,\rm keV}$[e] (erg $s^{-1}cm^{-2}$)	$L_{[0.5-2]\,\rm keV}$[f] (erg s^{-1})
1RXS J015530.4-085720	0.1336 ± 0.0269	222	2.14×10^{20}	$9.43 \times 10^{-13} \pm 1.90 \times 10^{-13}$	7.08×10^{43}
1RXS J091834.7+315632	0.0655 ± 0.0162	364	1.62×10^{20}	$3.99 \times 10^{-13} \pm 9.86 \times 10^{-14}$	3.01×10^{44}
1RXS J091930.5+110842	0.0749 ± 0.0191	323	2.78×10^{20}	$6.08 \times 10^{-13} \pm 1.55 \times 10^{-13}$	2.84×10^{44}
1RXH J092713.2+294334	0.0145 ± 0.0020	9056	1.75×10^{20}	$3.22 \times 10^{-13} \pm 4.45 \times 10^{-14}$	7.32×10^{44}
1RXH J092712.8+294344	0.0066 ± 0.0013	17 796	1.75×10^{20}	$1.48 \times 10^{-13} \pm 2.77 \times 10^{-14}$	3.36×10^{44}
1RXH J094214.9+090024	0.0056 ± 0.0012	5148	2.83×10^{20}	$1.42 \times 10^{-13} \pm 3.04 \times 10^{-14}$	1.88×10^{43}
1RXS J100022.3+223327	0.0476 ± 0.0138	335	2.57×10^{20}	$3.70 \times 10^{-13} \pm 1.08 \times 10^{-13}$	2.33×10^{44}
1RXS J101226.6+261335	0.0454 ± 0.0128	379	2.46×10^{20}	$3.45 \times 10^{-13} \pm 9.73 \times 10^{-14}$	1.71×10^{44}
1RXS J102736.8+605025	0.0320 ± 0.0095	631	7.00×10^{19}	$1.34 \times 10^{-13} \pm 3.96 \times 10^{-14}$	4.88×10^{43}
1RXS J110539.2+041449	0.0220 ± 0.0087	381	4.89×10^{20}	$2.37 \times 10^{-13} \pm 9.39 \times 10^{-14}$	1.64×10^{44}
1RXS J141441.9+165812	0.1424 ± 0.0218	412	1.19×10^{20}	$7.45 \times 10^{-13} \pm 1.14 \times 10^{-13}$	1.26×10^{44}
1RXS J153635.6+044118	0.0312 ± 0.0102	473	4.19×10^{20}	$3.13 \times 10^{-13} \pm 1.02 \times 10^{-13}$	1.66×10^{44}
1RXS J165256.4+312346	0.0205 ± 0.0076	647	2.56×10^{20}	$1.60 \times 10^{-13} \pm 5.88 \times 10^{-14}$	2.31×10^{44}
1RXS J171448.2+332737	0.0400 ± 0.0086	749	2.90×10^{20}	$3.32 \times 10^{-13} \pm 7.15 \times 10^{-14}$	3.06×10^{43}

Note. [a]ROSAT All-Sky Survey Catalogue source name.
[b]Count rates in the *ROSAT* band (0.1–2.4 keV).
[c]Exposure time.
[d]Galactic column density (Kalberla et al. 2005).
[e]X-ray fluxes at 0.5–2 keV calculated from the count rates in the *ROSAT* band by employing a power-law spectrum with a photon index $\Gamma = 2.0$ and corrected for Galactic absorption (Kalberla et al. 2005).
[f]Rest-frame luminosity in the 0.5–2 keV band (estimated from the unabsorbed X-ray flux).

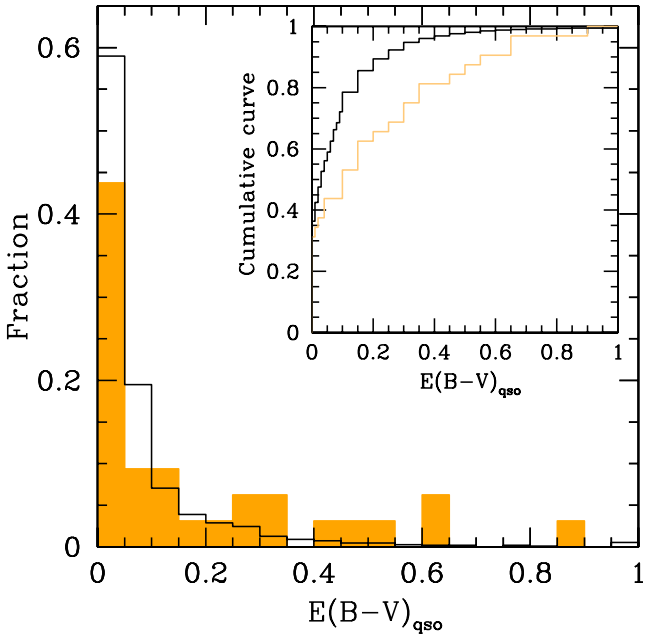

Figure 4. Disc reddening distribution for our sample (orange filled histogram) and for the control sample of typical QSOs (black open histogram). The two histograms are normalized to the total number of sources in the two samples. The internal panel shows the cumulative distributions of $E(B-V)_{\rm qso}$ for our sample (orange line) the control sample (black line).

Table 4. Average reddening values for the single classes.

$\langle E(B-V)_{\rm qso}\rangle$	σ	Median	Class	$N_{\rm obj}$
0.15	0.14	0.10	B	9[a]
0.13	0.10	0.10	D	3
0.24	0.21	0.30	A	5
0.26	0.30	0.02	O	15
0.20	0.24	0.1	Tot	32
0.08	0.14	0.03	Ref	1100

Note. a This sample contains objects with class B, BD, BA and BO.

and BBB in the case of high AGN reddening values, while the first is valid only in the case of redshift-matched samples. Nonetheless, winds can also contribute in modifying the shape of the SEDs providing obscuration in the optical–UV wavelength. Broad absorption line troughs in the bluest part of the C IV λ1550 and/or of the Mg II line could be used as an indicator of the possible presence of outflows. The C IV line is not covered by our SDSS spectra, while for the Mg II line we have sufficient coverage only for objects with redshift higher than ∼0.42 (seven objects, but two of those have $z \simeq 0.42$ where the bluest part is barely covered). However, there is no clear evidence of BAL troughs in the bluest part of this line.

8.4 Torus sizes and geometry

Based on equation (3), we estimated the size of the 12 μm emitting region in our sample and in the control sample. Results are shown in Fig. 7. The mean $s_{12\,\mu\rm m}$ for our sample is $\langle s_{12\,\mu\rm m}\rangle \simeq 11.6$ pc with a standard dispersion of 6.2 (the median $s_{12\,\mu\rm m}$ is 10.3 pc), while the control sample has a mean of 9.2 with $\sigma = 4.7$ (median

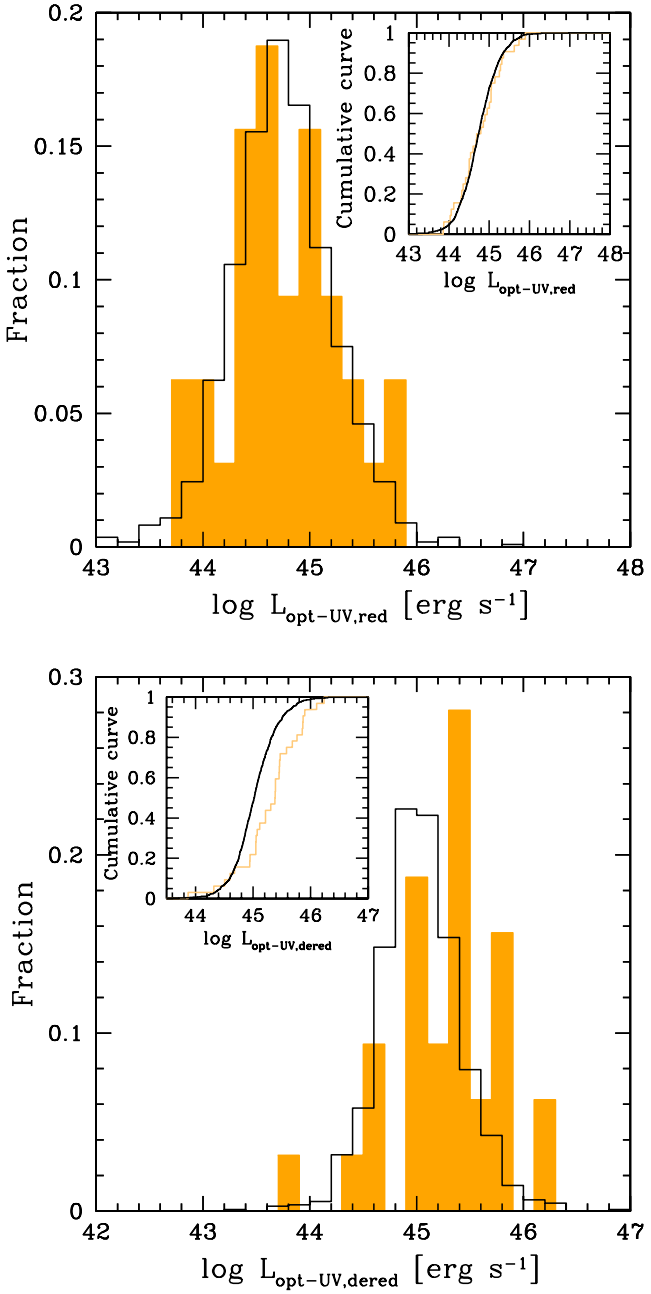

Figure 5. Disc luminosity distribution for our sample (orange filled histogram) and for the control sample of typical QSOs (black open histogram). The two histograms are normalized to the total number of sources in the two samples. The internal panels show the cumulative distributions for our sample (orange line) the control sample (black line). Top panel: Best-fitting disc luminosity before applying the reddening correction (host galaxy contamination removed). Bottom panel: Best-fitting disc luminosity after applying the reddening correction (host galaxy contamination removed).

$s_{12\,\mu\rm m} \simeq 8.2$ pc). The two samples are different at $\sim 2\sigma$ level from a K–S test.

If we assume that the torus is optically thick to its own radiation (e.g. Granato & Danese 1994; L13), the infrared emission along an equatorial line of sight (i.e. aligned with the torus) is smaller than along a polar line of sight. Sources with high reddening values (i.e. 18 out of 32 objects with $E(B-V)_{\rm qso} \geq 0.1$) are expected to have, on average, lower $L_{\rm ir}$ values, and thus lower $s_{12\,\mu\rm m}$ values. Yet, the

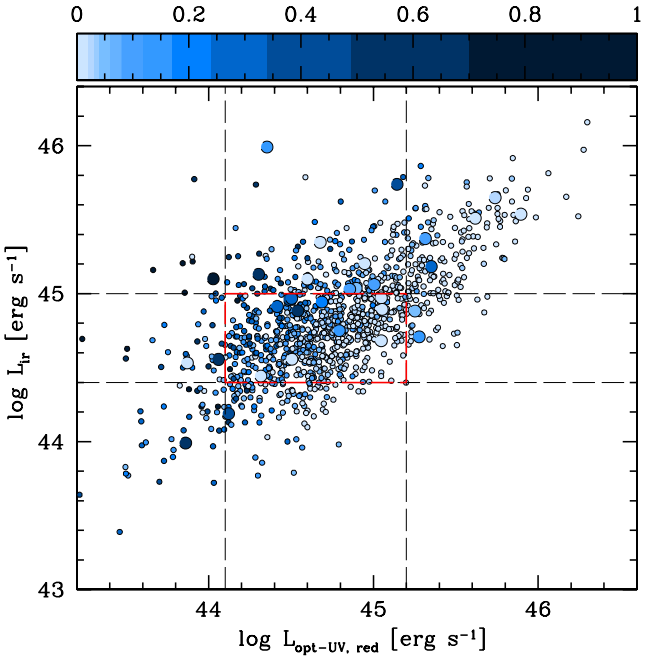

Figure 6. Infrared 'torus' luminosities as a function of disc 'accretion' luminosities (not corrected for reddening) for our sample (big circles) and for the control sample (small circles). The bluescale indicates the AGN reddening for each object: light blue represent low reddening (white means $E(B-V)_{\rm qso}=0$) and dark blue high reddening values (the darkest circles have $E(B-V)_{\rm qso}=1$). The red dashed lines encompass the region where the two samples have similar average $L_{\rm ir}$ and $L_{\rm opt-UV,red}$ values.

Table 5. Values of $L_{\rm ir}$, $L_{\rm opt-UV,red}$ and $E(B-V)_{\rm qso}$ for the control and our sample inside the region encompasses by the red dashed lines in Fig. 6 ($44.10 \leq \log L_{\rm opt-UV,red} \leq 45.20$ and $44.4 \leq \log L_{\rm ir} \leq 45.00$). This region has been selected in order to have luminosity-matched samples (within $\sim 1.6\sigma$).

Parameter	Median	Mean	σ
Our sample ($N=11$)			
$\log L_{\rm opt-UV,red}$	44.54	44.67	0.27
$\log L_{\rm ir}$	44.89	44.81	0.18
$E(B-V)_{\rm qso}$	0.15	0.17	0.21
Control sample ($N=596$)			
$\log L_{\rm opt-UV,red}$	44.69	44.68	0.27
$\log L_{\rm ir}$	44.72	44.72	0.16
$E(B-V)_{\rm qso}$	0.03	0.07	0.10

$s_{12\,\mu\rm m}$ values for our sample are marginally higher than the ones of the control sample. This is consistent with the larger intrinsic brightness (once we have corrected for reddening) in the optical (Suganuma et al. 2006; Mor, Netzer & Elitzur 2009) of our sample with respect to the control sample. In this scenario, inclination effects are not playing a major role in the optical AGN obscuration (otherwise we should observe lower $L_{\rm ir}$ and thus lower $s_{12\,\mu\rm m}$ values for an equatorial line of sight) under the assumption that the torus is optically thick. Inclination can still be a possible interpretation of the observed AGN obscuration if the torus is actually relatively optically thin to its own infrared radiation (this is consistent with the findings of L13, but see also Drouart et al. 2012). Another possibility is that our sample presents small-scale structure which is *intrinsically different* than the one of the control sample. More

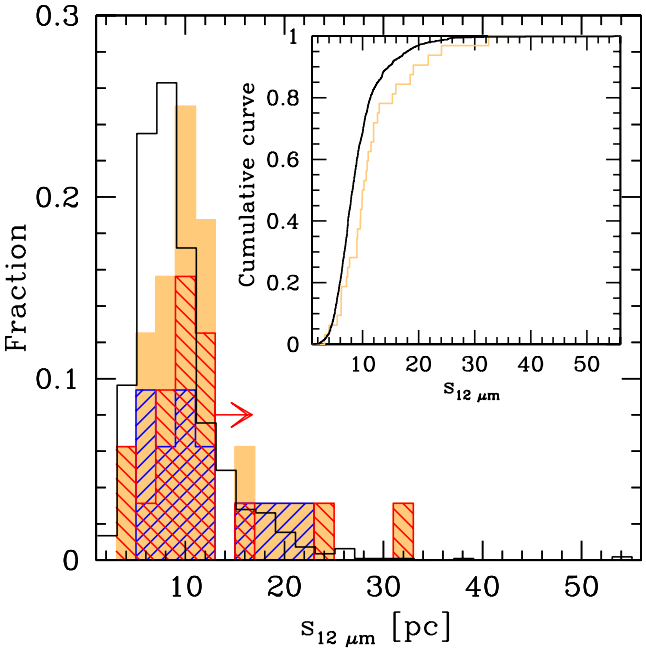

Figure 7. Distribution of the sizes (in parsec) of the 12 μm emitter for our sample (orange filled histogram) and for the control sample of typical QSOs (black open histogram). The two histograms are normalized to the total number of sources in the two samples. The red hatched histogram is the $s_{12\,\mu\rm m}$ distribution of our sample with $E(B-V)_{\rm qso} \geq 0.1$ (18 objects), while the blue hatched histogram is for our sample with $E(B-V)_{\rm qso} < 0.1$ (14 objects).

complex discs than the circular Keplerian disc, such as a warped disc, thought to occur around rotating BHs (Bardeen & Petterson 1975), may give rise to both obscuration and a wide range of line profiles (e.g. double-horned profiles; Bachev 1999; Zhang et al. 2009), but this is just a speculation and the current data do not yet place significant constraints on disc structure.

We can use the velocity difference between the broad and narrow emission lines together with the torus sizes to test the recoiling scenario. Through equation (2) we estimate the minimum BH mass ($M_{\rm min}$) required to keep the torus bound to a recoiling hole. To be as conservative as possible, we will assume that the candidate recoiling BH is actually moving exactly along the line of sight. For 28 out of the 32 objects in our sample BH masses ($M_{\rm Shen}$) has been estimated by Shen et al. (2011) through the single epoch method (e.g. Vestergaard & Peterson 2006). The result of this test is that $0.0001 < M_{\rm Shen}/M_{\rm min} < 0.2$ for 22 objects out of 28. For five objects $0.2 < M_{\rm Shen}/M_{\rm min} < 1$, and one object (J1652+3123) has $M_{\rm Shen}/M_{\rm min} \approx 2$. J1154+0134, the only object showing a reduced IR flux, is not among these six.

We note that (1) all the BH masses of these last six objects are inconsistent with the galaxy masses we estimate from the SED fitting. Even assuming that these objects are extreme outliers of the BH–host galaxy relations, (2) for two of them (J1027+6050 and J1105+0414) $M_{\rm min} > 10^{11}\,{\rm M}_{\odot}$ is required to keep the tori bound.[6] The unrealistic estimate of the BH masses for these two objects is caused by their double-peaked emitter nature, and single epoch measurements should not be attempted for the elements of

[6] Masses between 10^{10} and 10^{11} $\rm M_{\odot}$ are required for a recoiling BH to keep its torus for the four objects (J1207+0604, J1328-0129, J1440+3319 and J1539+3333) without mass estimates as well.

this peculiar class. The remaining four objects have $M_{\rm Shen}/M_{\rm min} \sim 1$ because of the very small velocity shifts measured, $\simeq$1000 km s^{-1} for all of them. None of these four objects have bell-shaped broad lines (i.e. they have not being classified as binary candidates), hence the simplest explanation is that these are standard AGN with slightly asymmetric lines.

We stress that in this test we neglected any projection effect. In the scenario of a recoiling BH with a 3D velocity inclined by 45° with respect to the line of sight $M_{\rm Shen}/M_{\rm min} < 1$ for the whole sample.

9 SUMMARY AND CONCLUSIONS

We have presented a homogeneous and comprehensive study of the broad-band properties of 32 quasars in the sample identified by Tsalmantza et al. (2011). These objects have been selected to have large velocity shifts (>1000 km s^{-1}) between NLs and BLs. According to the line profiles, source are subsequently divided in four classes: (1) fairly bell-shaped, strongly shifted BLs identify good BHB candidates; (2) BLs with evidence of double-horned profiles are classified as DPEs; (3) objects with asymmetric lines; (4) other sources with complex profiles, or having lines with relatively small shifts (∼1000 km s^{-1}).

One possible interpretation that might explain the BLs displacement is a recoil induced by the anisotropic emission of gravitational waves in the final merge of SMBHs pairs. This phenomenon would leave a characteristic imprint in the SED of these objects (i.e. a mid-infrared deficit). This analysis aims to investigate the multiwavelength SEDs of such peculiar QSOs, in particular in the context of the recoiling scenario depicted above.

To achieve this goal, we have employed the SED-fitting code already presented in Lusso et al. (2013), which models simultaneously three components of the AGN SED, i.e. hot-dust from the torus, optical–UV emission from the evolving stellar population and optical–UV from the accretion disc.

Our main findings are summarized in the following:

(1) All quasars analysed here present a significant amount of 12 μm emission. The SED of HDP quasars should be a further indication of displaced SMBH from the centre of a galaxy, maybe attributed to an undergoing recoil event. We do not find any evidence of such objects in the presented sample aside from J1154+0134, whose IR emission is a factor ∼10 lower than what expected from its UV–optical emission. Further follow-up (e.g. high-resolution imaging) is required to test the nature (recoil versus DPE) of J1154+0134.

(2) We find that our sample covers a wide range in terms of SED shapes with host galaxy contamination higher with respect to the QSO control sample (modulo degeneracies between the galaxy and a highly reddened BBB). Nevertheless, SEDs of our sample show, on average, moderately higher levels of intrinsic disc obscuration than the control sample (if we match solely on redshift).

(3) Disc luminosity estimates (before applying the reddening correction but host galaxy subtracted) for our sample and for the control one are not significantly different. Given the higher disc reddening contamination in our sample, then such objects should be intrinsically brighter than the QSO control sample.

(4) There is a tendency to have higher average sizes of the 12 μm emitter for our sample than the one for the control sample. This is consistent with the larger intrinsic (once we have corrected for reddening) brightness in the optical of our sample with respect to the control sample.

(5) If we assume that the torus is optically thick to its own radiation, the infrared emission observed from a line of sight aligned with the torus should be smaller than one along a polar direction. Sources with high reddening values (i.e. $E(B-V)_{\rm qso} \geq 0.1$) are expected to have lower $L_{\rm ir}$ values, and thus lower $s_{12\,\mu{\rm m}}$ values. However, we find that the $s_{12\,\mu{\rm m}}$ values for our sample are, on average, somewhat higher than the ones of the control sample. This indicates that inclination effects are not playing a major role in the optical AGN obscuration. The source of obscuration might be due to intrinsic differences in the small-scale structure of the quasars in our sample.

As a note of caution, we also point out that the difference in the average AGN reddening is no longer significant when we select a sub-sample in both our data set and the control sample with similar $L_{\rm opt-UV,red}$ and $L_{\rm ir}$. Moreover, objects classified BHB and DPEs in our sample have no significant difference in the intrinsic reddening even when compared to the larger control sample.

ACKNOWLEDGEMENTS

The authors acknowledge the anonymous reviewer who provided many useful suggestions for improving the paper. EL gratefully thanks Kate Rubin for useful discussions on galaxy outflows and Cristian Vignali for having reduced the *Chandra* and the *XMM–Newton* spectra of J0927+2943, J1328−0129, and J0155−0857, and for illuminating discussion on the X-ray properties of these sources. EL also thanks Joseph F. Hennawi, Gianni Zamorani, Andrea Comastri and the members of the ENIGMA group[7] at the Max Planck Institute for Astronomy (MPIA) for helpful discussions. MD and CM are grateful for the hospitality of the Max Planck Institute for Astronomy (MPIA). Support for MF was provided in part by NASA through Hubble Fellowship grant HF-51305.01-A awarded by the Space Telescope Science Institute, which is operated by the Association of Universities for Research in Astronomy, Inc., for NASA, under contract NAS 5-26555.

REFERENCES

Abazajian K. N. et al., 2009, ApJS, 182, 543
Bachev R., 1999, A&A, 348, 71
Baker J. G., Boggs W. D., Centrella J., Kelly B. J., McWilliams S. T., Miller M. C., van Meter J. R., 2007, ApJ, 668, 1140
Bardeen J. M., Petterson J. A., 1975, ApJ, 195, L65
Becker R. H., White R. L., Helfand D. J., 1995, ApJ, 450, 559
Begelman M. C., Blandford R. D., Rees M. J., 1980, Nature, 287, 307
Bentz M. C. et al., 2013, ApJ, 767, 149
Bogdanović T., Eracleous M., Sigurdsson S., 2009, ApJ, 697, 288
Boroson T. A., Lauer T. R., 2009, Nature, 458, 53
Bruzual G., Charlot S., 2003, MNRAS, 344, 1000
Calzetti D., Armus L., Bohlin R. C., Kinney A. L., Koornneef J., Storchi-Bergmann T., 2000, ApJ, 533, 682
Campanelli M., Lousto C. O., Zlochower Y., Merritt D., 2007a, Phys. Rev. Lett., 98, 231102
Campanelli M., Lousto C., Zlochower Y., Merritt D., 2007b, ApJ, 659, L5
Chabrier G., 2003, ApJ, 586, L133
Civano F. et al., 2012, ApJ, 752, 49
Civano F. et al., 2010, ApJ, 717, 209
Comerford J. M., Griffith R. L., Gerke B. F., Cooper M. C., Newman J. A., Davis M., Stern D., 2009, ApJ, 702, L82
Croom S. M., Smith R. J., Boyle B. J., Shanks T., Miller L., Outram P. J., Loaring N. S., 2004, MNRAS, 349, 1397

[7] http://www.mpia-hd.mpg.de/ENIGMA/

Cutri R. M. et al., 2003, 2MASS All Sky Catalog of Point Sources. NASA/IPAC Infrared Science Archive
Decarli R., Reynolds M. T., Dotti M., 2009, MNRAS, 397, 458
Decarli R., Dotti M., Fumagalli M., Tsalmantza P., Montuori C., Lusso E., Hogg D. W., Prochaska J. X., 2013, MNRAS, 433, 1492 (Paper I)
Dong X., Wang T., Wang J., Yuan W., Zhou H., Dai H., Zhang K., 2008, MNRAS, 383, 581
Dotti M., Montuori C., Decarli R., Volonteri M., Colpi M., Haardt F., 2009, MNRAS, 398, L73
Drouart G. et al., 2012, A&A, 548, A45
Elvis M. et al., 1994, ApJS, 95, 1
Elvis M. et al., 2012, ApJ, 759, 6
Eracleous M., Halpern J. P., 1994, ApJS, 90, 1
Eracleous M. et al., 2014, MNRAS, submitted
Eracleous M., Boroson T. A., Halpern J. P., Liu J., 2012, ApJS, 201, 23
Ferrarese L., Merritt D., 2000, ApJ, 539, L9
Flagey N., Boulanger F., Verstraete L., Miville Deschênes M. A., Noriega Crespo A., Reach W. T., 2006, A&A, 453, 969
Gaskell C. M., 1983, in Swings J.-P., ed., Proc. Liege Int. Astrophys. Colloq. Vol. 24, Quasars as Supermassive Binaries, Cointe-Ougree, Belgium, p. 473
Gaskell C. M., Ferland G. J., 1984, PASP, 96, 393
Granato G. L., Danese L., 1994, MNRAS, 268, 235
Guedes J., Madau P., Mayer L., Callegari S., 2011, ApJ, 729, 125
Gültekin K., Miller J. M., 2012, ApJ, 761, 90
Hao H. et al., 2010, ApJ, 724, L59 (H10)
Hao H., Elvis M., Civano F., Lawrence A., 2011, ApJ, 733, 108
Hao H. et al., 2013, MNRAS, 434, 3104
Hopkins P. F. et al., 2004, AJ, 128, 1112
Jiang L. et al., 2010, Nature, 464, 380
Ju W., Greene J. E., Rafikov R. R., Bickerton S. J., Badenes C., 2013, ApJ, 777, 44
Kalberla P. M. W., Burton W. B., Hartmann D., Arnal E. M., Bajaja E., Morras R., Pöppel W. G. L., 2005, A&A, 440, 775
Klaas U., Haas M., Heinrichsen I., Schulz B., 1997, A&A, 325, L21
Komossa S., 2012, Adv. Astron., 2012
Komossa S., Merritt D., 2008, ApJ, 689, L89
Komossa S., Zhou H., Lu H., 2008, ApJ, 678, L81
Kormendy J., Richstone D., 1995, ARA&A, 33, 581
Krawczyk C. M., Richards G. T., Mehta S. S., Vogeley M. S., Gallagher S. C., Leighly K. M., Ross N. P., Schneider D. P., 2013, ApJS, 206, 4 (K13)
Laor A., Draine B. T., 1993, ApJ, 402, 441
Liu X., Shen Y., Bian F., Loeb A., Tremaine S., 2013, preprint (arXiv:e-prints)
Lodato G., Nayakshin S., King A. R., Pringle J. E., 2009, MNRAS, 398, 1392
Lousto C. O., Zlochower Y., 2013, Phys. Rev. D, 87, 084027
Lousto C. O., Zlochower Y., Dotti M., Volonteri M., 2012, Phys. Rev. D, 85, 084015
Lusso E. et al., 2011, A&A, 534, A110
Lusso E. et al., 2012, MNRAS, 425, 623
Lusso E. et al., 2013, ApJ, 777, 86 (L13)
Lynden-Bell D., 1969, Nature, 223, 690
Magorrian J. et al., 1998, AJ, 115, 2285
Ma X.-C., Wang T.-G., 2013, MNRAS, 430, 3445
Marconi A., Hunt L. K., 2003, ApJ, 589, L21
Marconi A., Risaliti G., Gilli R., Hunt L. K., Maiolino R., Salvati M., 2004, MNRAS, 351, 169
Merritt D., Milosavljević M., 2005, Living Rev. Relativ., 8, 8
Mor R., Netzer H., Elitzur M., 2009, ApJ, 705, 298
Netzer H., 1982, MNRAS, 198, 589
Peres A., 1962, Phys. Rev., 128, 2471
Polletta M. et al., 2007, ApJ, 663, 81
Pozzi F. et al., 2007, A&A, 468, 603
Prevot M. L., Lequeux J., Prevot L., Maurice E., Rocca-Volmerange B., 1984, A&A, 132, 389
Richards G. T. et al., 2006, ApJS, 166, 470
Roche P. F., Aitken D. K., Smith C. H., Ward M. J., 1991, MNRAS, 248, 606
Rowan-Robinson M., Valtchanov I., Nandra K., 2009, MNRAS, 397, 1326
Salpeter E. E., 1964, ApJ, 140, 796
Salvato M. et al., 2009, ApJ, 690, 1250
Sanders D. B., Phinney E. S., Neugebauer G., Soifer B. T., Matthews K., 1989, ApJ, 347, 29
Sesana A., Roedig C., Reynolds M. T., Dotti M., 2012, MNRAS, 420, 860
Shang Z. et al., 2011, ApJS, 196, 2
Shen Y. et al., 2011, ApJS, 194, 45
Siebenmorgen R., Krügel E., Spoon H. W. W., 2004, A&A, 414, 123
Silva L., Granato G. L., Bressan A., Danese L., 1998, ApJ, 509, 103
Silva L., Maiolino R., Granato G. L., 2004, MNRAS, 355, 973
Suganuma M. et al., 2006, ApJ, 639, 46
Tanaka T., Menou K., Haiman Z., 2012, MNRAS, 420, 705
Treister E., Krolik J. H., Dullemond C., 2008, ApJ, 679, 140
Tremaine S. et al., 2002, ApJ, 574, 740
Tristram K. R. W. et al., 2009, A&A, 502, 67
Tristram K. R. W., Schartmann M., 2011, A&A, 531, A99
Tsalmantza P., Decarli R., Dotti M., Hogg D. W., 2011, ApJ, 738, 20
Vasudevan R. V., Fabian A. C., Gandhi P., Winter L. M., Mushotzky R. F., 2010, MNRAS, 402, 1081
Vestergaard M., Peterson B. M., 2006, ApJ, 641, 689
Voges W. et al., 1999, A&A, 349, 389
Wright E. L. et al., 2010, AJ, 140, 1868
York D. G. et al., 2000, AJ, 120, 1579
Zamojski M. A. et al., 2007, ApJS, 172, 468
Zhang X.-G., Dultzin D., Wang T.-G., Kauffmann G., 2009, MNRAS, 397, 1510

APPENDIX A: DETAILS ON THE SED-FITTING MODELS AND PROCEDURE

Our SED-fitting code models simultaneously three components in the quasar SED, i.e. hot-dust from the torus, emission from the evolving stellar population and emission from the accretion disc. The nuclear hot-dust SED templates are taken from Silva, Maiolino & Granato (2004). They were constructed from a large sample of Seyfert galaxies selected from the literature for which clear signatures of non-stellar nuclear emission were detected in the near-IR and mid-IR, and also using the radiative transfer code GRASIL (Silva et al. 1998). The infrared SEDs are divided into four intervals of absorption: $N_{\rm H} < 10^{22}$ cm^{-2} for Seyfert 1, $10^{22} < N_{\rm H} < 10^{23}$ cm^{-2}, $10^{23} < N_{\rm H} < 10^{24}$ cm^{-2} and $N_{\rm H} > 10^{24}$ cm^{-2} for Seyfert 2. Since all the objects in our sample are broad-line QSOs, the latter case is neglected in our analysis.

We employed a set of 18 galaxy templates built from the Bruzual & Charlot (2003) spectral synthesis models, built at solar metallicity and with a Chabrier IMF (Chabrier 2003). To make the galaxy templates representative of the entire luminous-AGN-hosting galaxy population, a set of models was selected with a range of star-formation histories (SFHs); the models combine six exponentially decaying SFHs with characteristic times ranging from $\tau = 0.1$ to 3 Gyr, with three total stellar-population ages of 6, 9 and 11 Gyr. For context, early-type galaxies (characterized by a small amount of ongoing star formation) are represented by the models with characteristic times $\tau < 1$ Gyr and old ages, whereas more actively star-forming galaxies are represented by models with larger characteristic times τ and smaller ages. An additional hard constraint applied to the fits is that, for each source, the only templates considered for fitting are those with total ages smaller than the age of the Universe (in our fiducial cosmological model) at the redshift of the source. Each template is reddened according to the Calzetti

et al. (2000) reddening law, with 11 permitted $E(B-V)_{\rm gal}$ values range between 0 and 0.5 with a step-size of 0.05.

The BBB template representative of the accretion disc emission is taken from Richards et al. (2006). The near-infrared bump is neglected since we have already covered the mid-infrared region of the SED with the hot-dust templates. This template is reddened according to the Prevot et al. (1984) reddening law for the Small Magellanic Clouds (SMC, which seems to be appropriate for type-1 AGN; Hopkins et al. 2004; Salvato et al. 2009). The AGN-reddening ($E(B-V)_{\rm qso}$) ranges between 0 and 1 with a variable step ($\Delta E(B-V)_{\rm qso}=0.01$ for $E(B-V)_{\rm qso}$ between 0 and 0.1, and $\Delta E(B-V)_{\rm qso}=0.05$ for $E(B-V)_{\rm qso}$ between 0.1 and 1.0) for a total of 29 templates.

The total number of free parameters in each of the linear fits is eight: three amplitudes corresponding to the three components involved in the fit, two parameters concerning the shape of the galaxy (i.e. τ and age), one parameter concerning the shape of the torus component, the AGN and the galaxy reddening.

We obtain approximate uncertainty estimates on model parameters by considering the variation in best-fitting χ^2 as a function of template property. In detail, the uncertainty estimate on each parameter x is produced by considering each alternative component combination, drawing a parabola in the space of x and χ^2 with a minimum at the best-fitting x and χ^2 but also passing through the alternative component combination's x and χ^2, and finding the x value where the parabola crosses $\Delta\chi^2=1$. From among these crossings (one per component combination), we use the most extreme values to determine the uncertainty estimates.

The resulting SED fits are presented in Fig. 1.

APPENDIX B: NOTES ON THE SED GENERAL PROPERTIES FOR THE DIFFERENT CLASSES

B1 Binary BH candidates and DPEs

BHB candidates (nine objects with class = B, plotted with filled circles in Fig. 2) and DPEs (three objects with class = D, marked with filled squares in Fig. 2) are almost all characterized by high host-galaxy contamination around 1 μm and AGN reddening lower than 0.5. J1050+3456 presents the highest reddening value in these two classes (i.e. $E(B-V)_{\rm qso}=0.45$ from the best fit, $E(B-V)_{\rm qso}\sim0.4$ from the mixing diagram), while J0927+2943 ($\alpha_{\rm OPT}=0.76$ and $\alpha_{\rm NIR}=-0.07$, marked with the green circle in Fig. 2) has rather standard AGN SED with little host galaxy contamination and no AGN reddening.

J1539+3333 is the only object that has been fitted with a galaxy template with very little contribution from the accretion disc. The optical spectrum of this source shows strongly shifted broad lines, no clear indication of [Ne V] is observed at any redshift which suggests modest or no AGN contribution in the optical–UV or strong extinction. The best-fitting SED of this source can be interpreted as the one of an obscured AGN; however, it is unclear whether *W*3 and *W*4 are powered by PAH feature as well. For this objects, *Herschel* data are necessary in order to disentangle between the torus or PAHs scenario.

B2 Asymmetric line profiles

Sources with lines in the optical spectra showing a symmetric base, centred at the redshift of the narrow lines, but an asymmetric core with a shifted peak are called *asymmetric* (class = A, five objects, see Paper I), and they are plotted with red triangles in Fig. 2. These AGN present both high host-galaxy contamination (∼70−90 per cent), and reddening ($0.3\lesssim E(B-V)_{\rm qso}\lesssim0.5$).

B3 Others

QSOs with complex line profiles or lines with small ($v_{\rm peak}\sim1000$ km s^{-1}) velocity shifts are marked as *others* (15 objects, marked as stars in Fig. 2). These sources cover a wide range of host galaxy contaminations and reddening.

For example, the best-fit of J1010+3725 ($\alpha_{\rm OPT}=-0.95$ and $\alpha_{\rm NIR}=-1.02$) shows conspicuous infrared emission compared with the BBB, with an SED similar to what has been observed in starburst/ultraluminous infrared galaxies (e.g. Arp 220, NGC 6240; Klaas et al. 1997). The AGN reddening value estimated from the mixing diagram ($E(B-V)_{\rm qso}\sim0.5$) is about 3.3 times higher than the one from the SED fit ($E(B-V)_{\rm qso}=0.15$). Hβ only, we cannot use the Hα/Hβ ratio. The high Hα/Hβ ratio observed in broad lines (see Paper I) may be a further hint of high extinction. Note however that the Hα/Hβ ratio in the BLR can be much larger than the case B recombination value of 3.0 usually adopted for narrow-line region (Gaskell & Ferland 1984) due to effects of high density and optical depth, and thus high Hα/Hβ ratios could not entirely be due to reddening of the BLR (Netzer 1982).

The spectrum of this AGN shows broadened [O III] (FWHM = 1140 km s^{-1}), with various components at different velocities, likely caused by massive gaseous outflows driven either by star formation or AGN winds. Such a feature is not observed in other lower ionization lines (e.g. [O II]).

J1215+4146 ($\alpha_{\rm OPT}=-2.20$ and $\alpha_{\rm NIR}=0.11$) presents the highest broad Hα/Hβ ratio in the sample (Hα/H$\beta\sim$20, see fig. 3 in Paper I), which might imply severe reddening (Dong et al. 2008), consistent with both SED best fit and mixing diagram estimates ($E(B-V)_{\rm qso}=0.90$). Note however that the same uncertainties discussed above for J1010+3725 apply here as well.

APPENDIX C: NOTES ON THE SED GENERAL PROPERTIES: *GALEX* DATA

GALEX data for the 10 sources with high host-galaxy contamination[8] described in Section 8.3 are usually too bright to be well fitted with the BBB template only and, in fact, a galaxy component in the optical–UV is required. An additional constraint on the contribution of the AGN to the UV emission could come from flux variability. As discussed in Section 3, only J0221+0101, J0829+2728 and J1440+3319 show significant variability (by a factor ∼2−3 in fluxes). The SED fitting of J0221+0101 and J0829+2728 requires a significant to dominant contribution of the AGN light to the UV spectrum, as it is expected for a varying object. The case of J1440+3319 is more subtle. Our SED analysis suggests that most of the UV emission comes from a young stellar population in the host, and such an origin would not justify the temporal behaviour of the quasar. To check whether the spectrum of J1440+3319 as well as of the others quasars with strong host contamination in the UV can be fitted with a BBB only we forced the analysis to assume low reddening values (i.e. we have imposed $E(B-V)_{\rm qso}\leq0.1$). In 4 objects (J1050+3456, J1215+4146, J1216+4159 and J1440+3319) out of 10, we have

[8] J0931+3204, J0942+0900, J1000+2233, J1050+3456, J1105+0414, J1207+0604, J1215+4146, J1216+4159, J1440+3319 and J1539+3333. The latter does not have any *GALEX* detection.

significant changes, in all other cases the mid-infrared to disc luminosity ratio is higher than 1, which is not physical (dust cannot reprocessed more optical–UV luminosity than what it is actually emitted from the disc). For J1215+4146, the disc component disappears and the photometry is well fitted solely by passive stellar population. We consider this fit unlikely, given that we have independent indications that this object is a red type-1 and the continuum should come from the AGN. J1050+0414 and J1216+4159 show better fits in the UV, nonetheless with high host-galaxy contamination in the near-IR/optical but, J1216+4159 presents mid-infrared to disc luminosity ratio close to one. Forcing low reddening value, the SDSS and *GALEX* data of J1440+3319 are well fitted by relatively young stellar population with an almost negligible disc component. Also in this case, the mid-infrared to disc luminosity ratio is higher than 1, making the interpretation of the J1440+3319 unclear. We stress however that, even if we consider these fits plausible, the difference between the reddening distribution of our and the control sample is still moderately significant at 2σ (instead of 2.7σ).

This paper has been typeset from a TEX/LATEX file prepared by the author.